GEORG-AUGUST-UNIVERSITÄT
GÖTTINGEN

Fakultät für
Physik

MAX-PLANCK-GESELLSCHAFT

Bachelor's Thesis

Velocity Distribution in a Granular Gas

Geschwindigkeitsverteilung in einem granularem Gas

prepared by

Jasper Ole Cirkel

from Göttingen

at the Max-Planck-Institute for Dynamics and Self-Organization

Thesis period:	9th August 2012 until 31st October 2012
First Referee:	Dr. Matthias Schröter
Second Referee:	Prof. Dr. Sarah Köster

Abstract

We create a granular gas composed of table tennis balls, and study their behaviour when being shaken vertically. Using techniques of digital particle image velocimetry (DPIV), the two-dimensional velocity distribution and anisotropy of temperature is of particular interest. A high speed camera is set up and supplied with enough lighting to illuminate balls moving at the order of metres per second ($\mathrm{m\,s^{-1}}$). A shaker provides vertical movement and different structured ground plates are used in order to excite the particles equally in all directions. The images are processed by a routine implemented in Matlab. We find that the velocity distribution is both dependent on the structure of the ground plate and the observed position in the container.

Zusammenfassung

Wir erstellen ein granulares Gas aus Tischtennisbällen in einem Plexiglaskasten und beobachten dieses, während es vertikal geschüttelt wird. Dabei werden Methoden der digitalen Partikel Bildverarbeitung (DPIV) verwendet um die Geschwindigkeitsverteilung und Anisotropie der Temperatur in zwei Dimensionen zu analysieren. Eine Hochgeschwindigkeitskamera mit entsprechender Beleuchtung filmt die Bälle, die sich in der Größenordnung von einigen Meter pro Sekunde bewegen. Eine Schüttelvorrichtung sorgt für vertikale Bewegung und unterschiedlich strukturierte Bodenplatten regen die Bälle in alle Richtungen an. Die Bilder werden mit einem Matlab-Programm verarbeitet. Wir zeigen, dass die Geschwindigkeitsverteilung sowohl von der gewählten Bodenplatte, als auch von der beobachteten Position in der Box abhängt.

Contents

1. Introduction **1**

2. Model **3**

2.1. Granular Gas 3

2.1.1. Granular Temperature and Velocity Distribution 3

2.2. Coefficient of Restitution ϵ 5

3. Experimental Setup **7**

3.1. Shaker 7

3.2. Acrylic Glass Box 8

3.3. Ground Plates 9

3.4. Measuring the Acceleration 11

3.5. Balls 12

3.6. Camera 12

3.6.1. Position of the Camera 13

3.7. Lighting 14

3.8. Coefficient of Restitution ϵ 17

4. Image Processing **19**

4.1. Overview 19

4.2. Background division 21

4.3. Binarisation 24

4.4. Erosion 26

4.5. Particle Detection 27

4.5.1. Treating of Large Regions 30

4.6. Evaluating Velocity Vectors 31

4.7. Exemplary Entering of a Ball 32

4.8. Subimage handling 35

4.9. Error of Image Processing Procedure 35
4.9.1. Error of Distance 35
4.9.2. Error of Absolute Position 37
4.9.3. Error of Velocities 39
4.10. Box Counting 40

5. Results **43**
5.1. Statistical Validity 43
5.2. Particle Density 44
5.3. Velocity Distribution 51
5.3.1. Spatial Velocity Distributions v_x and v_y 52
5.3.2. The Velocity Distribution v_z 54
5.3.3. Temperature and Velocity Distribution 57
5.4. Flow Field 59
5.5. Anisotropy of Temperature 59

6. Discussion **63**
6.1. Coefficient of Restitution 63
6.2. Image Processing 63
6.3. Particle Density 64
6.4. Velocity Distribution 64
6.4.1. The Velocity Distribution v_z 65
6.4.2. Temperature 66
6.5. Anisotropy 67
6.6. Conclusion 67

7. Outlook and Future Work **69**

A. Supplementary Figures **73**

B. Supplementary Tables **77**

1. Introduction

In general, the model of a granular gas applies to any dilute accumulation of particles over a certain size. Interestingly, such a conglomeration of macroscopic bodies exhibits characteristics which are commonly attributed to molecular gases. On the one hand, this means that most classical ideas, concepts and tools can be applied to study and analyse such a gas. In fact, the main differences are the spatial dimensions which of course influence other properties, but the main physical concepts and laws remain. Therefore, it is not surprising that some of the terminology such as mean free path was used to describe granular materials.

On the other hand, the conceptual proximity did not seem to stimulate the development in the field of granular gases until the late seventies of the last century [8]. Maybe the idea that a characteristic which was seen as intrinsic to microscopic materials, could also be present on larger scales seemed more of a conceptual challenge to researchers than the conceptual proximity aided their understanding. Nevertheless, a quote from a paper by Albert Einstein illustrates the idea that only the length scale separates the main characteristic of microscopic and macroscopic concepts [4]: "a dissolved molecule is differentiated from a suspended body *solely* by its dimensions".

Temperature, for example, is a characteristic of the surrounding world which has a determining role in everyday life. However, the definition of temperature—mainly deriving from motion and rotation—seems to be restricted to the molecular length scale. Therefore, it might seem striking that a system composed of macroscopic particles such as the table tennis balls used in this experiment actually features an identical or at least analogous definition of this characteristic, and that this definition leads to an improved understanding of the particles' collective properties.

Whereas the study of microscopic systems is difficult because of challenging length scales, the investigation of macroscopic systems can be achieved with relative ease. For the design of an experiment, it might be extraordinarily helpful to have the opportunity to confirm the initial measurements by hand or by eye to rule out any

major conceptual measurement difficulties.

This is certainly true in the case of particle image velocimetry. Here, consecutive images are analysed to determine the trajectory of particles. It is hard to image that anyone would argue in favour of analysing hundreds - or even more - images by hand. However, one has to bear in mind that this was the common experimental method before powerful computer and programs were available to aid the experimenter.

While the physics behind granular media somewhat reinvent or retrace the steps of classical physics, the digital particle image velocimetry (DPIV) tries to emulate the properties and competence of human vision and its object identification skills.

The aim of this Work is to establish the experimental conditions for a granular gas. Table tennis balls are shaken vertically with two different ground plates which excite the particles in all directions. Key element of the measuring process is a high speed camera. The raw data is composed of numerous digital images, and is investigated utilising an image processing routine developed taking advantage of the methods provided by Matlab. The velocity distribution of the gas leads to its temperature and is the main focus of the data analysis.

In the next Chapter we will introduce a theoretical model for granular gases. Chapter 3 deals with the experimental setup and Chapter 4 explains the image processing routine. In Chapter 5, the results are presented and in Chapter 6 follows a discussion. An outlook to possible future work is given in Chapter 7.

2. Model

2.1. Granular Gas

The model of granular material applies to any conglomeration of discrete, macroscopic, solid bodies which lose (or better said, transform) energy upon every contact. Granular material with low particle density and infrequent contact between the particles can be modelled as a granular gas. Whereas a hypothetical granular gas with elastic contacts behaves mostly like a molecular gas, any real system featuring inelastic collisions shows qualitatively different behaviour [7]. A high particle density leads to uniform behaviour of the gas with all particles acting as a whole [5, 11]. While some characteristics remain analogous to the molecular case, others, such as the velocity distribution show a behaviour which can only be described with classical methods as a first approach. The amount of inelasticity of the inter-particle collisions is, among others, the major source of different behaviour because the gas particles are macroscopic bodies with further degrees of freedom [2].

2.1.1. Granular Temperature and Velocity Distribution

In analogy to regular gases, the granular temperature of a granular gas of identical particles of mass m can be defined [2] as:

$$\frac{3}{2}T := \frac{m}{2}v_T^2, \tag{2.1}$$

where v_T is the thermal velocity given by $\vec{c} := \vec{v}/v_T$. The temperature has the following relation to the velocity distribution function $f(\vec{v})$ and its second moment [1, 2]:

$$\frac{3}{2}nT = \int d\vec{v}\frac{mv^2}{2} \cdot f(\vec{v}),$$

where $n = N/V$ is the particle density. This term, including the velocity distribution, has to be kept in a constant form over time in order to maintain a constant

temperature. For a granular gas in an equilibrium state, the second moment $\langle v^2 \rangle$ is an indicator of the temperature. However, if the cooling process can be understood as slow enough to be a sequence of equilibriums states, the change of temperature might be regarded analogous to adiabatic cooling [2].

The velocity distribution function f can be written in a the scaled form [2]:

$$f(\vec{v}) = \frac{n}{v_t^3} \tilde{f}(\vec{c}).$$

The assumption that particle collisions are only slightly inelastic leads to the reuse of the classical Maxwell velocity distribution which might be represented [2] as:

$$\phi(c) := \pi^{-3/2} \exp(-c^2).$$

A first improvement, taking the inelastic contacts into account, is the Sonine polynomial expansion S_P [1] with coefficients $\{a_i\}_{i\in}$:

$$\tilde{f}(c) = \phi(c) \left(1 + \sum_{p=1}^{\infty} a_p S_p(c^2) \right)$$

The first three functions of the orthogonal system in three dimensions read:

$$\begin{aligned} S_0(x) &= 1 \\ S_1(x) &= -x + \frac{3}{2} \\ S_2(x) &= \frac{x^2}{2} - \frac{5}{2}x + \frac{18}{5}, \end{aligned}$$

and it can be shown analytically [2] that $a_0 = 1,\ a_1 = 0$ and:

$$a_2 = \frac{16(1-\epsilon)(1-2\epsilon^2)}{81 - 17\epsilon + 30\epsilon^2(1-\epsilon)} \tag{2.2}$$

is the first non trivial coefficient. ϵ describes the coefficient of restitution discussed in in the following Section.

Experimentally, there are several possible ways to excite, or *heat*, a granular gas. For example, the vibration of a vertical cylinder or a slightly tilted plane with exciting walls [11] might provide the dissipated energy to the particles.

2.2. Coefficient of Restitution ϵ

The foundation of the theoretical view on the topic of granular dynamics is based on the collision of two identical spheres with velocities named v_1 and v_2 undergoing their contact with a relative movement of $v_{12} := v_1 - v_2 > 0$. Ideal objects would lose no kinetic energy due to contact, however, it is interesting to specify the amount of lost, or transformed, energy. This property is quantified by the so-called coefficient of restitution ϵ [2]:

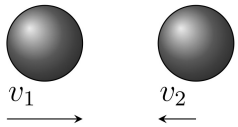

Figure 2.1.: Two colliding spheres characterised by their respective velocities v_1 and v_2. Drawn after [2].

$$\epsilon := -\frac{v'_{12}}{v_{12}},$$

where v_{12} denotes the relative movement of two colliding spheres before the contact whereas the prime sign $'$ specifies the velocity after the collision. However, this definition is not easily accessible to an experimental setup as velocities are sometimes difficult to measure. In order to define a property for a single object, the collision with an ideally elastic static plane is considered, and the coefficient of restitution becomes the fraction of initial and velocity after the impact:

$$\epsilon := -\frac{v'}{v}.$$

Possible values for ϵ range between 1 and 0, where $\epsilon = 1$ relates to an ideal elastic object, and $\epsilon = 0$ means the object does not bounce off the ideal plane.

For an approach to measure the value of ϵ, consider dropping a ball off a specified height H and observing the regained maximal height after the collision h. Using $E_{kin} = 1/2mv^2 \Leftrightarrow v = \sqrt{\frac{E_{kin}}{m}}$ the coefficient rewrites as follows:

$$\epsilon := -\frac{v'}{v} = \frac{\sqrt{\frac{E'_{kin}}{m}}}{\sqrt{\frac{E_{kin}}{m}}} = \sqrt{\frac{E'_{pot}}{E_{pot}}} = \sqrt{\frac{mgh}{mgH}} = \sqrt{\frac{h}{H}}. \tag{2.3}$$

For the third to last step, the equality of kinetic and potential energy at the specified heights is needed.

The value of ϵ is not constant for all velocities [2], however, the dependency can be neglected for the range of velocities triggered in this experiment.

3. Experimental Setup

3.1. Shaker

The shaker has the function to provide the necessary vertical movement for the balls to fly through the container. The *tira vibrational system TV 5800/LS* was originally designed as an industrial system to test all kinds of components under dynamic stress. The basic principle of the shaker is based on the force F on an electromagnetic coil exposed to an constant magnetic flux density B:

$$F(t) = B \cdot I(t), \tag{3.1}$$

where $I(t)$ is the (time dependant) current. The maximal possible force of course depends on the amount of mass and the frequency.

The shaker converts the electric input into a vertical physical movement which can extend up to a total of 50.8 mm. The system consists of several parts. Two linear power amplifiers amplify an external signal. One also acts as the control unit monitoring the operation. The external signal is provided by a frequency generator. It was run in sinusoidal mode only and it was experimentally found that any frequency lower than roughly 30 Hz does not shake the balls, whereas using over 50 Hz vibrates the box too much, and intense sounds are the consequence. Therefore, it was decided to run the experiments at a frequency $f \approx 30\,\mathrm{Hz}$. An air blower is needed in order to dissipate the an amount of $500\,\mathrm{m}^3\,\mathrm{h}^{-1}$ of warm air while operating under full load to the outside. The air is added to the system by a stationary pressurised air supply of 400 kPa to 600 kPa.

The amplitude of the external frequency is the main parameter varying the acceleration of the shaker which is clear from Equation (3.1). The control unit for the shaker has a turning knob to control the internal gain as well. However, it is only useful for temporarily quieting the shaker inbetween experimental runs, and then turn it to its maximum again, because it does not allow for precise adjustment of

Figure 3.1.: View of the experimental setup. 1 Shaker, 2 acrylic glass box, 3 camera, 4 power amplifier, 5 air tube, 6 air blower, 7 halogen floodlight, 8 paper.

the shaking current. The momentary current can be read on the control unit, and is adjusted by carefully turning the knob of the frequency generator. The shaker delays any adjustment made by a few tenth of a second and tends to alter the current slightly after a few seconds or even minutes. This happens especially if the gain control is moved. Therefore it might be difficult to hold a constant current.

The shaker can be run with a current of up to roughly 105 A. Choosing currents for the experiment was based on the lowest value that would allow for the balls to move around in a good part (majority of particles reach at least half the height) of the box. This was achieved by manual observation of images before the image processing was implemented. A value of 45 A was found sufficient, and its double 90 A was chosen as the maximum. 60 A and 75 A are used as further points of measurement as well.

3.2. Acrylic Glass Box

The function of the acrylic glass container is to simply hold the balls during the experiment and allow for them to move around in the inside. It measures $560 \times 305 \times 400\,\mathrm{mm}^3$ on the inside. It is constructed using an aluminium framework with acrylic glass windows to four sides. The bottom consist of a rigid aluminium plate. Since the

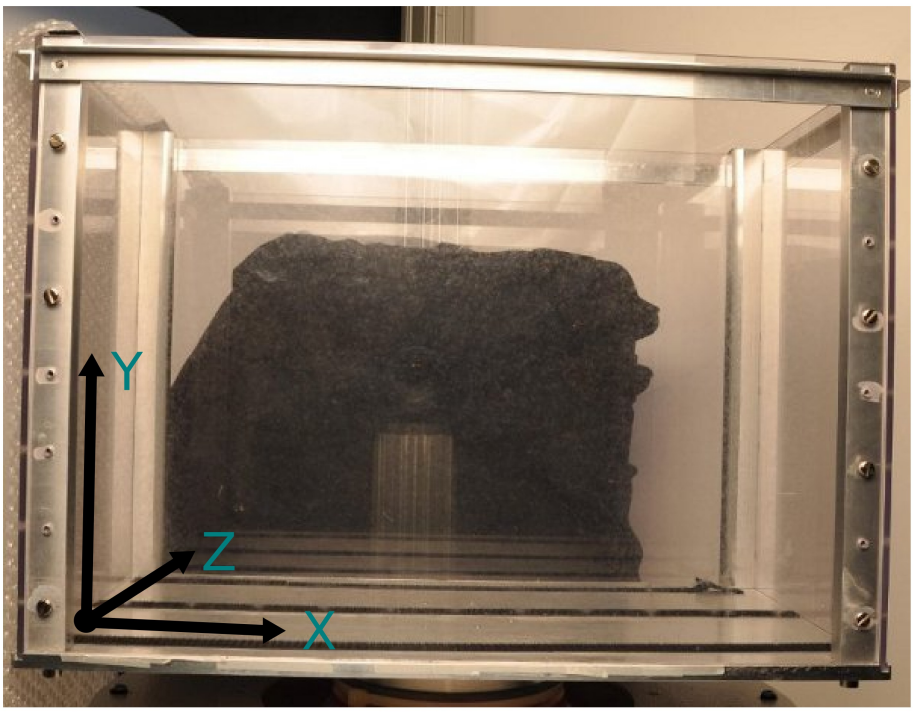

Figure 3.2.: View of the acrylic glass box with the coordinate system used.

observation of the balls is done from the front at least this side has to be clear. The kinetic energy of balls being rather low it is sufficient to have a cardboard top or bubble wrap attached with little segments of hook and loop tape. Bubble wrap lets in some light from the top and the box can easily be opened by de-attaching it at only one or two corners. A smaller box (half the height) was originally constructed for another, older project so that all windows were in a new, unused condition.

A measurement with a digital level confirmed the ground of the box is plane. In a central z-position it was inclined by $(0.00 \pm 0.05)^\circ$. Positioning the level diagonally, the inclination read $(0.05 \pm 0.05)^\circ$. The box is screwed to the underlying shaker in the middle, thus, if the ground plate is not rigid enough, this should be primarily noticeable on the sides.

3.3. Ground Plates

A plane and even ground would accelerate particles mainly vertical—because the shaker itself provides movement in this direction. In order to stimulate the other spatial directions as well, ground plates triggering this kind of movement through their structure are necessary. They should feature no predominant direction in the

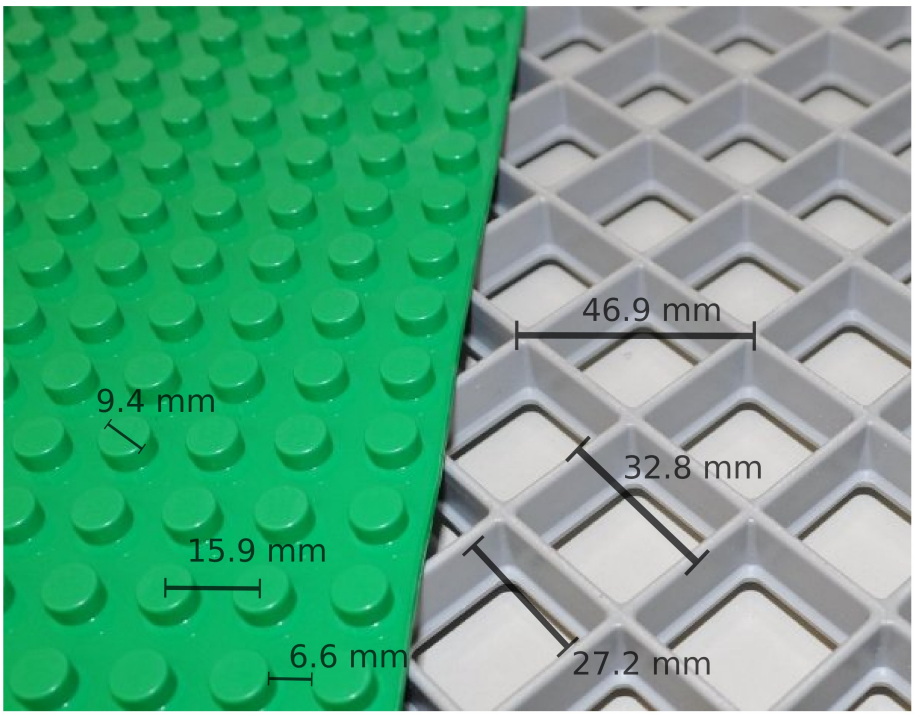

Figure 3.3.: View of the two ground plates used in the experiment.

	inclination [°]				
ground plate	front	centre	back	diagonal ↘	diagonal ↗
large structure	(0.00 ± 0.05)	(0.1 ± 0.1)	(0.2 ± 0.1)	(0.2 ± 0.1)	(0.2 ± 0.1)
small structure	(0.05 ± 0.05)	(0.1 ± 0.1)	(0.1 ± 0.1)	(0.2 ± 0.1)	(0.3 ± 0.1)

Table 3.1.: Inclination measured for the ground plates.

x-y-plane. For the experiment, the acrylic glass box is equipped with either of the following ground plates depicted in Figure 3.3. The small structured plate (green) is a standard *Lego Duplo* ground plate for children. The large structured ground plate (grey) was cut out of the bottom plane of a standard commercial storage box. Both plates could be installed in the box with three lines of hook and loop tape. However, the grey ground plate offers less area for adhesive bonding, and it roughly lasted long enough for half of the time it was used.

Unfortunately, the even level of the metal ground plate is not reached when the structured ground plates are attached. The values given in Table 3.1 show a very slight inclination. This might be due to the tape between the metal and the structured plates because the structured plates themselves are plane.

3.4. Measuring the Acceleration

The information about the current used to run the shaker does not directly provide the actual acceleration a of the entire box which is physically more interesting. In order to gain this information, an acceleration sensor was placed in five different positions on the metal ground plate. The shaker was run with four currents ranging from 45 A to 90 A. An accelerometer of type *Kistler 8702B100* pictured in Figure 3.4 measures a voltage which can be converted to an actual acceleration using a conversion factor f unique to the particular sensor; $f = 49.76\,\mathrm{mVg}$ where g is the standard acceleration of gravity[1] $\mathrm{g}{=}9.807\,\mathrm{m\,s^{-2}}$.

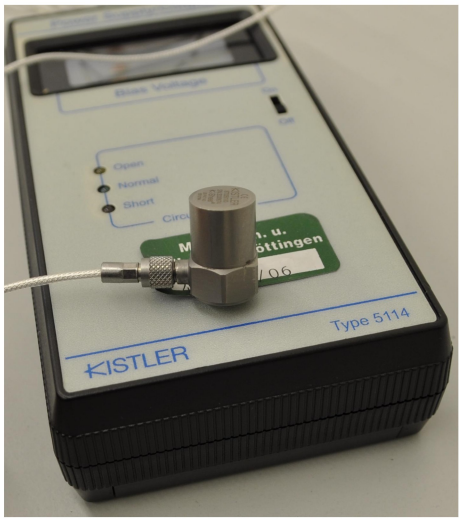

Figure 3.4.: The acceleration sensor with the control unit.

The sensor was attached on the ground of the container in five different positions with double sided adhesive tape to investigate the homogeneity of the acceleration. This examines, how vibrating on the open ends of the box affects the acceleration in comparison to the value in the centre where the box is attached to the shaker. The retrieved signal is a voltage of sinusoidal form because the acceleration of the box alternates with the sinusoidal signal provided. It can be visualised and analysed with a standard oscilloscope. A sinus fit function is useful as the signal is not purely sinusoidal and not entirely constant over multiple periods. Double peaks were observed and might be caused by vibration of the attached cables. Moreover, vibrations within the tape might cause some noise in the signal.

From the measurements documented in Table B.1 (p. 78) an acceleration could be assigned to each of the currents used in the experiment as shown in Table 3.2 (p. 12). In the following the experiments, run under a certain current will be indicated by those values. The dependency seems to be almost linear with an factor close to 10.

[1] This value is used to calibrate the sensor.

shaking amplitude $I\,[A]$	acceleration $a\,[g]$
45	4.6 ± 0.1
60	6.0 ± 0.2
75	7.6 ± 0.3
90	8.8 ± 0.2

Table 3.2.: Average values for the acceleration a on the metal ground plate of the acrylic glass box. The error is given by the standard deviation of the values given in Table B.1 (p. 78)

3.5. Balls

Standard commercial table tennis balls are chosen as particles for usage in the experiment. They are lightweight (2.6 g) and, therefore, relatively easy to accelerate. The white colour is useful for the image processing procedure. Moreover, these particles are available in industrial quality[2] and quantity. Regular *joola* so-called three star competition balls are used in the experiment which bear a blue and black brand sign. The darker area of the brand sign can affect the image processing. The usage of cheaper balls was tried—not because of the price—but because of their lack of a brand sign. However, their rougher surface causes large (order of mm^2) scratches on the acrylic glass windows even when touching slightly. Instead the *joola* balls only leave small (order of $1/10\,\mathrm{mm}^2$) dots on the glass when touching the glass with considerable force. Nevertheless, after completion of the experimental phase, the windows were somewhat blurry from scratches and an undamaged margin of the ball's radius was clearly visible.

3.6. Camera

The camera is the vital part of the image acquisition process. To be able to keep track of particles moving with velocities in the range of metres per second, a high speed camera with exposure times and image taking frequency in an adequate range is needed. A *pco.1200s*-camera with a *cmos*-sensor[3] is utilised in the experiment. The lens used is a *Nikon AF Nikkor* with a focal length of 50 mm and possible

[2] A leaflet, [9], published by the International Table Tennis Federation defines weight ((2.67 to 2.77) g and a 24 balls sample shall not have more than a 0.03 g standard deviation), diameter ((39.50 to 40.50) mm). Moreover, the documents sets standards for *sphericity* (below 0.35 mm) and *bounce conformity* (see Section 3.8 (p. 17)).

[3] An image sensor mainly consisting of a complementary metal–oxide–semiconductor.

apertures of 1.8 up to 22. The camera is chosen to operate in black/white modus, thus, the images contain no colour information. The highest quality images which can be selected in the firmware called *CamWare* are 16bit greyscale images in the *tif*-format[4]. Greyscale refers to an image where each pixel only holds intensity information. The value can be understood as a measure of photon count up to a certain limit. Grey values range from 0 meaning black or not enough photons to trigger the sensor at this pixel to $2^{16} - 1$ for white.

The camera can be programmed to film as long as internal memory is available, then replacing the first saved image. Simultaneously, it transfers the data to the connected computer. The number of images expected for a single experimental run, however, is so high that it is advisable to store many images in a single file which is possible with so called multi frame *tiff*s. Nevertheless, there seems to be a limit to the file size on the computer's system, only allowing 817 frames to be saved into one image file. The largest, or longest, continuous image sequence was, therefore, chosen to have this length.

3.6.1. Position of the Camera

Although it yields some advantages to film the entire acrylic glass box at once, for the experiment two considerably smaller positions were chosen to be filmed and analysed. The advantage of filming the entire box is that, ideally, all particles are visible at all times. This would make it easier to study the overall behaviour of the balls. Furthermore, it even allows for the image processing to utilise the maximum number of balls as a parameter for locating the balls.

However, the entire container is shaking up and down (50.8 mm) during the the experiment, thus, the images of the static camera would contain large parts of the structure of the box such as the aluminium bottom. In turn, this would certainly add complexity to the processing steps. Moreover, another practical problem lies in the necessary distance between the box's front window and the lens of the camera; to view the entire box, this distance roughly equates to 2 m which would cause the camera to be stationed well outside the frame constructed around the shaker. In turn, this would lead to the need for additional structures to block light around the camera's line of vision.

Therefore, one central and one border view are chosen. These views, or positions,

[4]Acronym for tagged image file format; used because of its lossless compression.

name of position	x[mm]	y[mm]	width [mm]	height [mm]
border	65	190	210	170
centre	205	190	210	170

Table 3.3.: Positions of the camera's image on the front window of the container.

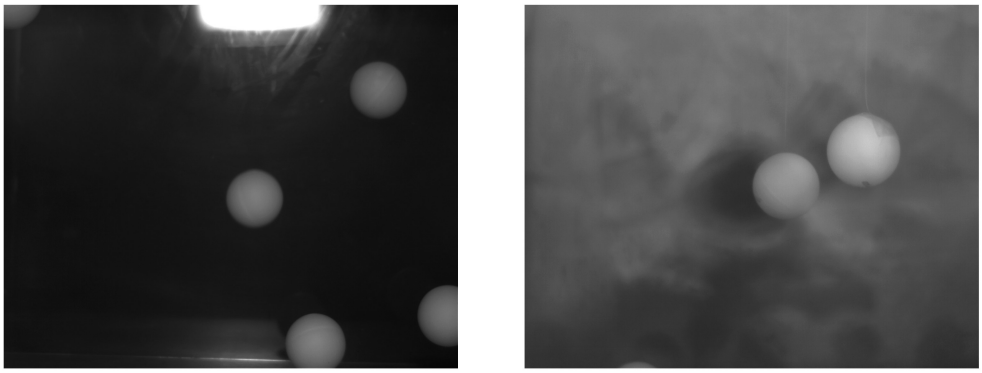

(a) (b)

Figure 3.5.: (a) A Floodlight points directly to the front window of the box. This causes a strong reflection from the centre of the floodlight. (b) The black hole in the centre of the image is the camera lens and the the wrinkled structure is paper surrounding it. This image was edited to be bright enough for printer settings.

account to the values in Table 3.3 and are given in the coordinate system shown in Figure 3.2 (p. 9). A certain overlap of the positions is useful to test whether the data found at the right margin of the border position continuously, and thus consistently, connects to the data found at the central position's left margin.

3.7. Lighting

The shaker is located in a basement room, under the single ceiling window of the room. Thus, the illumination situation is severely influenced by changes of natural lighting conditions outside. Because these changes can occur quite fast—and often—there seemed to be no option to manually adjust for example the aperture of the lens; the need for fairly stable luminosity conditions triggered the construction of a framework around the shaker to block most natural light. The framework was constructed of 80 mm×80 mm aluminium profile beams. The entire construction around the shaker measures approximately 2 m×2 m×2.5 m and is equipped with black felt tissue on all open sides.

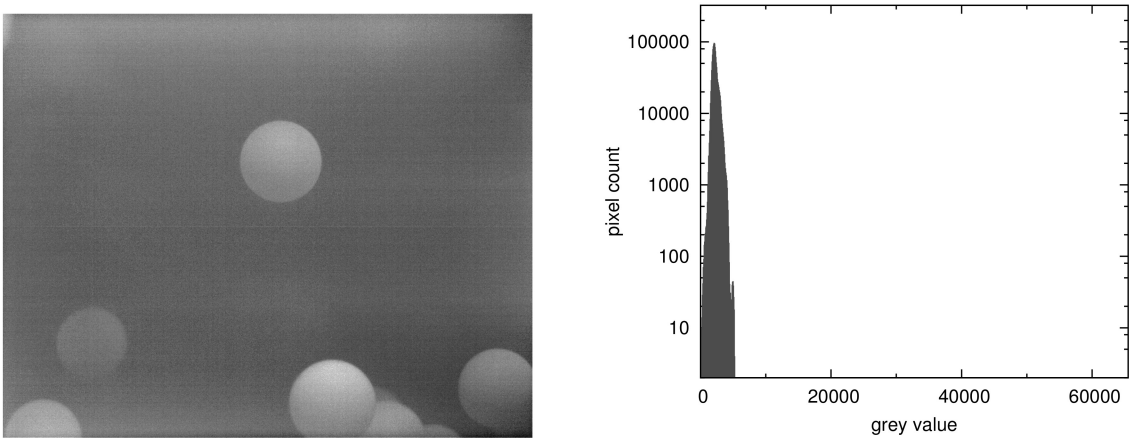

(a) (b)

Figure 3.6.: (a) Image taken with one floodlight aiming at the top of the framebox. Although the eye is able to distinguish balls, the overall luminosity is low. (b) The histogram of the image on the left stresses the lighting conditions; only a small fraction ($\approx 1/10$) of the possible 16 bit range is used.

As a consequence, an intense artificial light source is necessary. All light directly depending on the standard power supply suffer under the 50 Hz modulation. Thus, some other concepts were considered. A 28 by 56 components led panel available in the institute running on a laboratory power supply did not provide enough luminosity to take images with exposure times in the millisecond range. Even with an increased general gain for the camera's sensor the images remained dark with short exposure times. Another alternative are battery powered led panels used in professional photography, however, they seem too expensive as multiple ones are probably needed. Employing a stroboscope was also considered, but its frequency would have to be synchronised exactly with the camera.

A less expensive light source are simple commercial halogen floodlights which providing plenty of luminosity which is why this option was finally chosen. A disadvantage is the heat development; they heat up very quickly which makes it difficult to readjust them for testing purposes. The use of a simple air fan reduced the time of cooling enormously.

In the initial setup a single halogen floodlight was aimed directly at the front window of the acrylic glass box. The problem with this setup is the uneven distribution of light and a strong reflection from the centre of the light source which can be seen in figure 3.5. A plate made for diffusing light did not decrease the effect sufficiently.

Figure 3.7.: Final set up of the lighting with two halogen floodlight and and large reflective poster. The positions of both, the camera and the container are indicated because they are not shown in the image itself.

Using indirect lighting reflecting from a bright, but not to reflective surface, was considered. A first approach can be seen in figure 3.1 (p. 8). Here, the floodlight is aimed at the top of the framework where a large poster was pinned over the black felt tissue. The reflection of the light source were effectively decreased, however, the overall luminosity remained too low. Increasing the overall gain of the camera's sensor only resulted in highly noisy images. The insufficiency of the setup can be noticed by comparing the image in figure 3.6 (p. 15) and its histogram. The image itself seems noisy and some of the balls can hardly be distinguished by the eye. The lower margin of the leftmost complete ball is hardly visible. The histogram shows that the overall luminosity is low, as no pixel triggers a value above roughly 7000. Only a tenth of the possible range is occupied and it would be difficult to separate particles from background.

In order to improve the luminosity, a poster was also placed around the the camera lens and the floodlight was adjusted to illuminate this poster. This had the undesired result of the camera itself being reflected, most likely on the front window. An image of this situation is shown in figure 3.5 (p. 14). Obviously, this setup is not suitable because the background of the image is uneven and because of the amount of reflection.

Removing the poster around the camera lens up to the point where it caused no reflection and pointing the floodlight on the lower part of the paper helped reduce reflection enormously. The luminosity was improved in comparison to pointing the light to the top. The distribution of light was fairly even, however, the overall luminosity was not sufficient enough. Still, the grey values of balls and background were too close together to reliably separate balls from background. Hence, an additional floodlight was installed yielding the final setup for the lighting; Placement of the two floodlights above the box glaring against a large paper above the camera and reflecting back to the container. The camera is surrounded by black tissue. The final setup of the lighting is depicted in Figure 3.7 (p. 16).

The finalisation of the lighting also provides the opportunity to determine the exposure time of the camera for the entire experiment. First of all, the aperture was set to maximise the light gain. Experimentally, it was found that an exposure of roughly 2 ms provides enough luminosity for the balls to be distinguishable and the borders not to be too blurred by the movement occurring within this time interval. In addition, a pause lasting 6 ms was inserted. As a consequence, the might balls *jump* to their next position if they are fast, but for most balls, the movement remains small. Too little movement might also introduce problems because errors in the image processing might lead to wrong detection of the direction of the velocity if the movement is in the same order as the expected error. Moreover, fewer images can be analysed in order to span a necessary time period for the observation.

3.8. Coefficient of Restitution ϵ

To measure the coefficient of restitution ϵ of the balls used in the experiment a sample of four different balls, two already used in the shaker, and one new, are dropped from a height of approximately 20 cm onto a rigid 2 cm metal plate. Three to four series are recorded per ball. Using the extremal positions of the ball position and Equation 2.3 (p. 5), it is possible to obtain a value for $\epsilon = \sqrt{\frac{h}{H}}$. The measurement is carried out manually by choosing a rectangular selection around the ball with an image viewing program, thereby obtaining upper left corner coordinates, width and height to calculate the ball's centre.

The weighted value $\bar{\epsilon}$ of all measurements displayed in Table B.7 (p. 82) accounts

to:

$$\overline{\epsilon} = (0.930 \pm 0.002),$$

and Gauss error law yields the error $\sigma_{\overline{\epsilon}}$:

$$\sigma_{\overline{\epsilon}} = \sqrt{\left(\frac{1}{H^2} \cdot \sigma_h\right)^2 + \left(\frac{h}{H^2} \cdot \sigma_H\right)^2}, \tag{3.2}$$

where $\sigma_{h,H}$[5] is obtained from:

$$\sigma_{h,H}^2 = \sigma_{ground\ position}^2 + \sigma_{climax\ position}^2. \tag{3.3}$$

The values of $\sigma_{ground,climax\ position}$ are estimates based on the quality of the images, i.e. how precise the manually measured coordinates are. The ITTF[6]-publication [9] already mentioned in Section 3.5 (p. 12) sets the following standard; a ball dropped from a height of 305 mm shall bounce up to 240 mm to 240 mm which is equivalent to an $\epsilon_{ITTF} \in [0.887; 0.923]$. The measured value slightly exceeds the specification.

The data of Table B.7 (p. 82) implies that the value of ϵ is not altered by the usage in the shaker. Therefore, it is possible to use balls rather unlimited and it is not necessary to exchange the whole set of balls at once.

The found value of ϵ corresponds to a Sonine-coefficient of $a_2 = -0.012$ using Equation (2.2) (p. 4).

[5] σ_H stands for the error of the (higher) first height (H), and σ_h for error of the consecutive (lower) extremal position (h).

[6] Acronym for International Table Tennis Federation

4. Image Processing

4.1. Overview

The aim of the image processing procedure is to extract the information about position and velocity of the balls indirectly included in the images. The program for this project was entirely developed using Matlab and its *Image Processing Toolbox*, an extension providing numerous routines for image analysis and manipulation. Although these routines can undoubtedly produce surprisingly good results it is, nevertheless, important to bear in mind that any simplification or improvement achieved by the experimental setup itself while acquiring the image enormously decreases the effort needed for the computational process. This can be seen in figure 4.1 where the human eye can easily detect two balls, however, the lower one would be rather difficult to find with image processing.

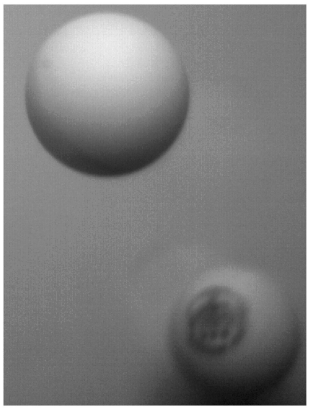

Figure 4.1.: Two balls in front of a white background

It is certainly positive to have an even coloured background in the images handed over to the image processing step as any gradient in colour would require more post processing. Working with a dark or preferably black background, seems even more suitable when observing bright particles such as white table tennis balls. In the resulting image the particles should appear brighter and the remaining rest would be considerably darker. In this setup a standard plastic box layered with black felt tissue was placed behind the acrylic glass box. This minimises reflections from light passing through the container.

Nonetheless, one might also consider an entirely white background because the reflection would brighten the image overall, and depreciate the effect of shadows between the particles. In the light Section (Section 3.7, p. 14) it was discussed that gaining enough photons per area for an exposure time of few milliseconds is difficult.

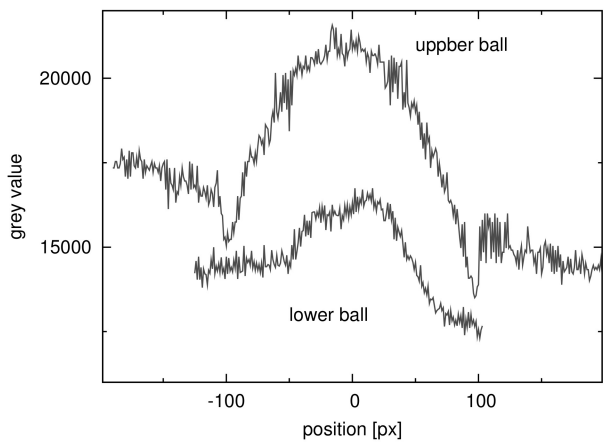

Figure 4.2.: For the upper ball the grey values drop at the margin of the ball, before they increase above the level of the surrounding background. The lower ball, however, is hardly detectable as a maximum. Its border edge is not distinguishable.

What further dismisses the concept of a bright background is the fact that reflection on the side of the ball, which is perpendicular to the camera chip, reflects less light than the parallel plane of the background itself. The border of the upper ball in Figure 4.1 (p. 19) is actually not an edge from low to high greyvalues, but rather from low to lower, to high grey values as shown in the plot of the grey values in Figure 4.2. The lower ball is visible, but its position can hardly be determined by looking at the grey value data.

An image and grey value distribution of a ball taken with black background is shown in figure 4.3. The ball can easily be located because of the sharply defined increase in greyvalue when the area of the ball is reached. This is a good starting point for successful image processing.

The process of image processing in this project can be separated into the following steps:

1. Background division
2. Binarisation
3. Erosion
4. Detecting of balls
5. Evaluating velocity vectors

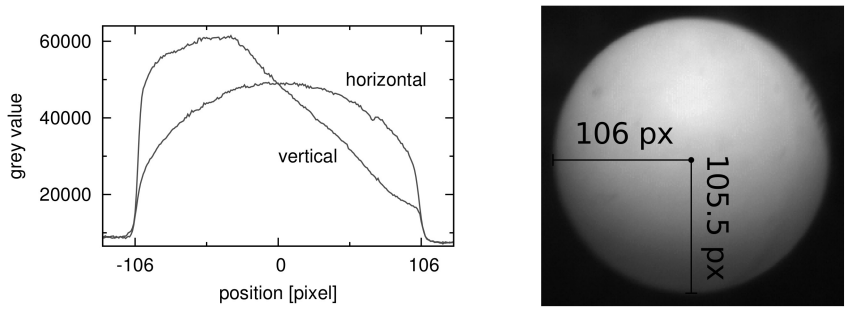

(a) (b)

Figure 4.3.: Intensity value profile (a) for one ball (b) decreasing towards the lower margin. Increasing position values correspond to moving down and right. The sharp increase, however, initiates just before the physical border of the ball is reached.

4.2. Background division

Division of an image by another image means to divide the corresponding intensities pixelwise. In this case the actual image is divided by the background image. The background image is obtained by evaluating the mean value of 400 images filmed without balls and a white sheet of paper attached to the back of the container. Ideally, this setup allows for any impurities (e.g large scratches) on the box's windows to show up in the background image and remove them through division. One has to bear in mind that the background images are taken without shaking the filmed box. Shaking is not necessary because it would only make sense to do so if in turn the physical position of the shaker and the box would somehow be synchronised with the image acquired by the static camera.

For the mean background shown in figure 4.4 (p. 22), the intensity decreases in vertical direction (rows) whereas the trend of the data is more symmetric for the horizontal averages of the columns. The scratch visible inside the circle, however, is to small to be noticed in the plot of the average intensity values in figure 4.5a (p. 23).

The Matlab program for this project reads in the 16 bit frames, and before the division of the background image the original image, with its 16 bit integer greyvalue, is converted to double precision. In a following step, the brightest pixel is detected and the entire image is linearly transformed so that the brightest pixel holds the largest possible value for the 16 bit integer image (65535) used in the consecutive processing steps. This ensures the use of the entire range available, and moreover,

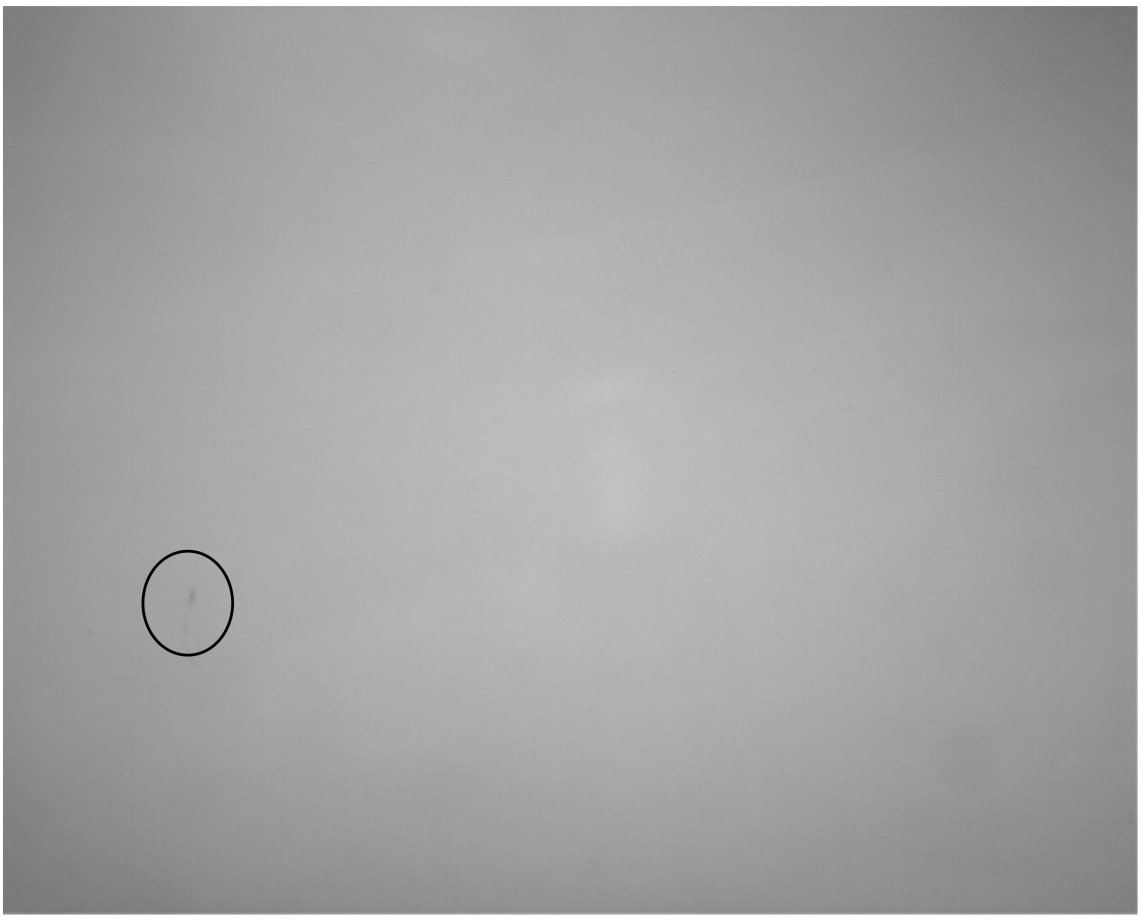

Figure 4.4.: Mean background image over 400 frames taken in a central position with a sheet of white paper behind the back window of the box. A large scratch on the acrylic glass is highlighted inside the circle.

the reconversion to integer quality suffers less under rounding errors. Furthermore, it reduces the problematic fact that the the overall grey values vary with the voltage modulation. Maximum and average grey value plotted in Figure 4.6 and display a clear periodicity.

Another Matlab program handles the generation of the background images based on a sample of 400 image frames. In the procedure, a single frame is added to a temporary image of type 32 bit double to avoid overflow of added values. This is done by the imadd and as a consecutive step imdivide carries out the division by the number of frames before reconversion to a greyscale format.

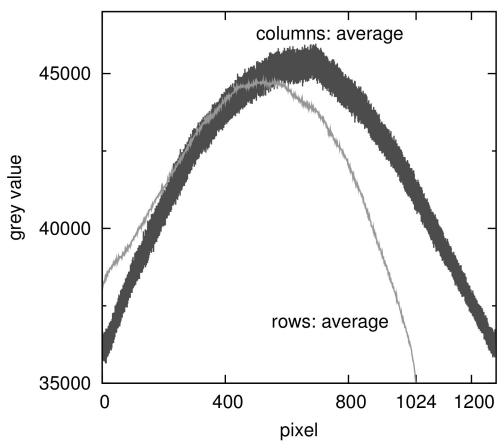

(a) The mean grey value of a white background is decreasing towards the margins of the image. This effect is only symmetric for the horizontal direction. The image shows a significant brighter top.

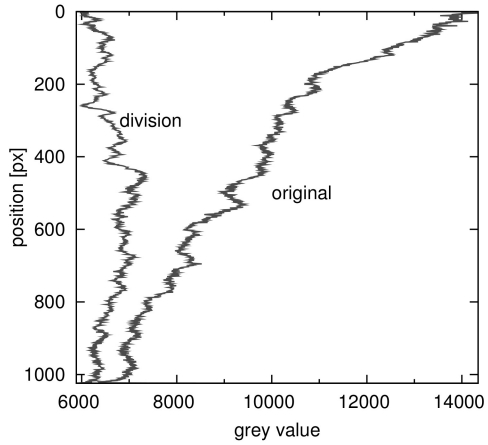

(b) The background division effectively decreases the vertical gradient. The grey values in the original image are significantly higher at the top of the image (position=0 px), however, the division results a smother profile. The profile shows the horizontal mean over a region without balls.

Figure 4.5.

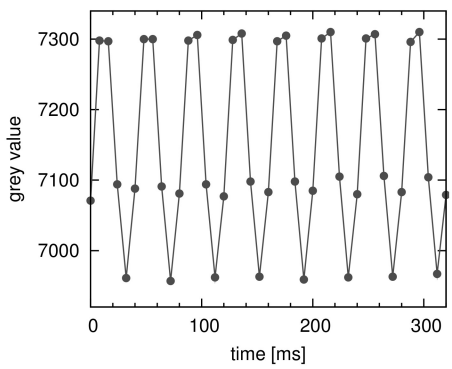

(a)

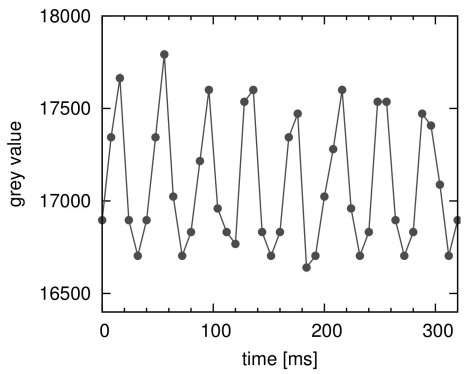

(b)

Figure 4.6.: The mean (a) and maximum (b) greyvalues computed for consecutive images clearly display a periodicity.

4.3. Binarisation

To binarise an image or, more broadly any type of data, means to apply a step-like function $f_{threshold}$ determining whether a value is above or below a certain threshold value $v_{threshold}$. The data which is above the threshold value is marked as 1, and the data below as 0:

$$f_{threshold}(v) = \begin{cases} 1 & v \geq v_{threshold} \\ 0 & v \leq v_{threshold} \end{cases} = \delta(v - v_{threshold}).$$

For the case of this Work, this means greyscale images are turned into binary images where each pixel has either value 1, representing white or value 1 which appears black. Ideally any pixel belonging to the background would be marked with a value of 0 and only those areas which can be attributed to a ball would be binarised to a 1. For few images the modulation of the light source leads to such high grey values that a small margin on the top of the image is also converted to white. Since these areas usually have a very slim shape it is not difficult to distinguish between a margin and a ball. Nevertheless, this represents a source of error when a ball is located in this region and the white areas overlap.

There are two reasons why finding a global threshold value is a difficult task in the case of this experiment. First, the overall mean grey value differs with the slight change of the the light intensity caused by the 50 Hz modulation of the electric system. Moreover, the grey values significantly decrease in the vertical direction. This effect is plotted in Figure 4.10 (p. 30) for the border position. It can lead to a situation where the background intensity is actually higher than the darker areas on the margin of a ball placed on the bottom of the acrylic glass box. Division by a suitable background image can, however, help normalise the overall distribution of the intensity values as displayed in Figure 4.5b.

Because the balls are viewed from one direction their spherical shape causes significantly less light to be reflected in the areas of the ball that appear to be the margins of the circle in the image. Thus, the grey values are higher in the centre of the ball. The Intensity value distribution for one ball is not entirely symmetric as can be seen in Figure 4.3 (p. 21). This ball was positioned in the right third of the screen and approximately at half the height. The effect of the light coming from above causes the grey value to rise to its maximum even before the centre of the ball. Below the position of the maximum, the values are decreasing linearly until

the edge of the ball.

A dynamic approach to find the best threshold value $v_{threshold}$ for each frame would be superior to setting the value manually. One way is the method of Otsu [12] implemented in the routine graythresh, however, it did not yield particularly good results for the images used in this Work. This methods evaluates $v_{threshold}$ based on an idea to minimise the variance of the grey values within each of the two classes created by the cut of the binarisation. The images of the balls are problematic because their grey values differ heavily. The comparison of figure 4.3 (p. 21) and 4.10 (p. 30) shows that the difference between the extremal values of the ball is significantly higher than the difference between the ball's minimum and the background's maximum value. The background values lie roughly between 6000 and 14000. The ball spans a much wider range from 14500 to just over 60000. Caused by the circumstances of the image taking process, the variance is higher in the ball and the approach to minimise it does not seem feasible in the case of the experiment. Therefore, it is not surprising to find that Otsu's method yields a higher $v_{threshold}$ than needed. Furthermore, another problems arises when a particular image features very few or no parts of a ball. The method would nevertheless estimate a value to separate particles and background leading to a situation where large portions of the background are thought to be particles. However, if no ball is present in the image there is no need to find a dynamic threshold. This would call for an algorithm to evaluate whether any, or how many balls are to be expected in the image. This problem might be approached by summing all grey values and therewith estimating the number of balls. For an image with some particles present Otsu usually yields a value being to high by a factor of 1.5 to 2. Bearing this in mind, it seemed more suitable to set the threshold manually, based on the grey values on the border of sample balls.

Doing this, it is important to notice that the sudden intensity increase displayed in figure 4.3 (p. 21) is not located exactly at the physical border of the particle. The increase noticed outside of the ball might be due to multiple reasons. First of all, the ball is moving during the exposure time. Under ideal lighting conditions this should even allow for an estimation of the particle's direction because the border should be sharper on the sides perpendicular to the movement. Obviously, this information would remain unsigned, i.e. without sense of direction. Secondly, the depth of sharpness blurs the image of balls not exactly positioned in the focused plane. Furthermore, light is reflected from the borders of the ball so that a slim

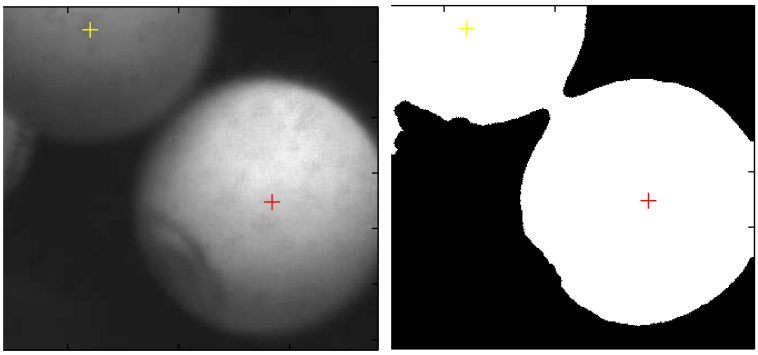

(a) original image (b) binary image

Figure 4.7.: The two adjacent balls a physically detached, however, the grey value between them is higher than $v_{threshold}$. Therefore, they seem to be connected in the binary image. This is the binary image passed to the subimage function, thus, the original binary image was already eroded once.

$$
\begin{matrix}
1 & 1 & 1 & 1 & 1 & 1 & 1 \\
1 & 1 & 1 & 1 & 1 & 1 & 0 \\
1 & 1 & 1 & 1 & 1 & 1 & 0 \\
1 & 1 & 1 & 1 & 0 & 0 & 0 \\
1 & 1 & 1 & 1 & 1 & 0 & 0 \\
1 & 1 & 1 & 0 & 0 & 0 & 0 \\
0 & 0 & 0 & 0 & 0 & 0 & 0
\end{matrix}
\rightsquigarrow
\begin{matrix}
1 & 1 & 1 & 1 & 1 & 0 & 0 \\
1 & 1 & 1 & 1 & 1 & 0 & 0 \\
1 & 1 & 1 & 0 & 0 & 0 & 0 \\
1 & 1 & 1 & 0 & 0 & 0 & 0 \\
1 & 1 & 0 & 0 & 0 & 0 & 0 \\
0 & 0 & 0 & 0 & 0 & 0 & 0 \\
0 & 0 & 0 & 0 & 0 & 0 & 0
\end{matrix}
$$

Figure 4.8.: Erosion of a binary image with a 2 by 2 structuring element with origin in the circled grid point in the left part results in the binary image on the right. The operation on this particular point would erode all three highlighted ones because of the mismatching zero.

margin around the ball seems brighter as well. This effect is especially important to particles positioned close to each other, but not touching each other. The reflection brightens the resulting image between the balls even if the line connecting them is almost perpendicular to the line of vision. Thus, in some cases, it can be observed that physically detached particles form a connected area in the binarised image. An example of the effect is displayed in Figure 4.7 (p. 26).

4.4. Erosion

Erosion is a fundamental technique in image processing. To erode an image, one has to define an object to erode with, often called structuring element, which is a

binary image itself. For every white pixel in the original image, it is tested whether the structure element lies completely inside the white region surrounding the pixel. More precisely, whether every pixel of the structuring element marked with a 1 for white matches a white pixel in the original image. However, this might only be important for fragmented structuring elements. If the matching-test is positive, the image remains unchanged. If this is not the case, the pixel and all white pixel of the structuring element are stripped off the original image, i.e. their values are turned to black or 0. In Figure 4.8 the structuring element is a 2 by 2 square indicated in red.

Mathematically two-dimensional binary erosion can be defined as follows. Let E be the integer grid ^{2} and I be a binary image in E. The structuring element might be called S, and its translation to any point on the grid is $S_z = \{s+z|s \in S\}, \forall z \in Z$. Erosion operates on I and results in the eroded image I_{eroded}:

$$I_{eroded} = I \ominus S = \{z \in Z|S_z \subseteq I\}$$

For this project, the structure element is provided by a Matlab routine named strel. The element is a so-called disk, i.e. the object closest to a circle in the integer grid ^{2}. By observing numerous images produced by the experimental set-up, a radius of 6 pixel was found sufficient to erase small impurities off the image. Those impurities include little areas, or even single pixels, not belonging to a ball which were nevertheless binarised to a value of 1. To the Matlab function a radius of 6, however, means what one might expect to be a radius of 7, so a radius of 0 creates a single point. Therefore, the structure element eroding the images obtained in the experiment might be represented as depicted in figure 4.9. The routine receiving the binary images then starts out by eroding the entire image with this structure element using the built-in function imerode.

4.5. Particle Detection

The detection of particles is based on properties of connected white pixel regions in the eroded binary image. The regions are labelled by the routine bwlabel assigning an increasing integer to every area beginning in the upper left corner. If a flag for visual debugging is set, a separate image with coloured region is also created for improved visual distinction. Consecutively, the Matlab function regionprops provides

```
0 0 0 0 0 0 1 0 0 0 0 0 0
0 0 0 1 1 1 1 1 1 1 0 0 0
0 0 1 1 1 1 1 1 1 1 1 0 0
0 1 1 1 1 1 1 1 1 1 1 1 0
0 1 1 1 1 1 1 1 1 1 1 1 0
0 1 1 1 1 1 1 1 1 1 1 1 0
1 1 1 1 1 1 1 1 1 1 1 1 1
0 1 1 1 1 1 1 1 1 1 1 1 0
0 1 1 1 1 1 1 1 1 1 1 1 0
0 1 1 1 1 1 1 1 1 1 1 1 0
0 0 1 1 1 1 1 1 1 1 1 0 0
0 0 0 1 1 1 1 1 1 1 1 0 0
0 0 0 0 0 0 1 0 0 0 0 0 0
```

Figure 4.9.: Structure element, used for erosion of the entire image, with a radius of 6 px which results in an binary image with a 13 px diameter.

the following information about every region:

- area: size of the region in pixels
- centroid: the center of mass (COM) of the region. The COM is the unweighted average of the pixel coordinates contained in the region. For an ideal ball that shows up as an ideal circle in the binary image, the COM points to its centre. However, for less symmetric shapes, the COM is usually more viable information in comparison to the centre of the bounding box (see below).
- bounding box: the coordinates of the upper left corner of a rectangle containing the region, and its width and height
- weighted centroid: like centroid, however, the COM is weighted with the grey values of the divided original image. Because the balls are generally brighter above their centre as shown in Figure 4.3 (p. 21), the weighted COM is shifted upwards in the region and, therefore, a less viable information about the particle position.
- maximal intensity: the maximal grey value of the region.

Looping through the regions, the decision whether it should be qualified as a ball is based on the above information as follows. The area shall range between a minimal and maximal area; these are computed with regard to the erosion because an ideal ball is stripped off twice the radius of the structure element:

$$area_{max} = f_{area_{max}} \cdot \pi(radius_{max,initial} - 2 \cdot radius_{structure\ elment})^2 \tag{4.1}$$

The factor $f_{area_{max}} = 1.1$ is used to adjust small impurities in the binary image. $radius_{max,initial}$ is the radius of a ball at the front window of the acrylic glass box, i.e. the largest possible radius without erosion. $radius_{structure\ elment}$ stands for the radius of the structure element discussed in Section 4.4 (p. 26). The minimum value for the area of a region is evaluated analogous, however, using the the diameter of a ball positioned at the back of the container, thus appearing small. Furthermore, the width and height of the bounding box shall be below a maximal and above a minimal value because these two properties are dependant on the radius of the ball. This is computed similar to the area boundaries. Moreover, the ratio of width and hight which indicates the bounding box's squareness is tested:

$$\frac{width}{height} < f_{squareness}$$

This fraction and its inverse is tested with $f_{squareness} = 1.2$. The penultimate requirement for a region to be classified as a ball is a test of roundness. As width and height of the bounding box should correspond to the diameter of a ball, the area measured by the regionprops function should be close to the area computed with width and height:

$$\pi \cdot (0.5 \cdot min(width,\ height))^2 < f_{roundness} \cdot area$$

Here, $min()$ takes the minimum of its arguments, area is the area returned by regionprops and $f_{roundness} \approx 1$ is an empirical factor for both the upper and lower limit of the roundness area.

In a final step, the maximal intensity value should be above a certain boundary set to $min_{intensity} = 25000$. This seems suitable when comparing the value with the plot of the maximum values of a black background in Figure 4.10 and the typical grey values of a ball in figure 4.3 (p. 21).

If a region fulfils the above requirements, it is marked as being a ball and the following data is stored to an array. The centroid position is saved as the potential position of the particle. The width and height have to be modified in order to represent the diameter of the ball because the erosion took away a certain part. This is important to notice since the ball size in the image, and ,therefore, the diameter too, vary strongly with depth. Consider for example the extreme situation where the diameter at front window equals 240 px and is roughly 170 px at the back window. Omitting this information would introduce an error up to a factor of

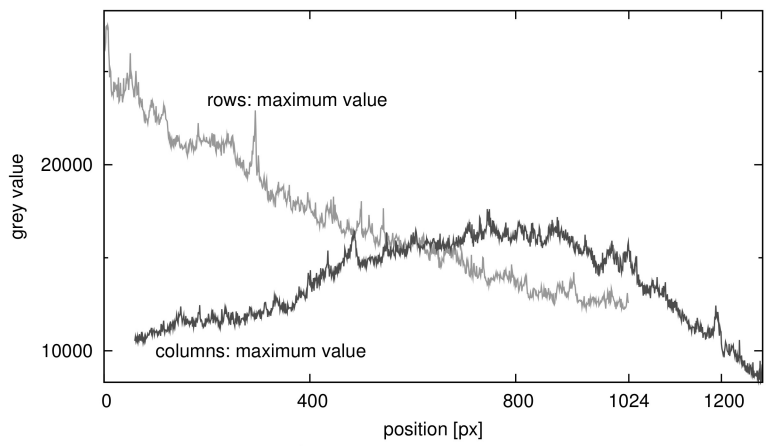

Figure 4.10.: The maximum value of the black background in the border position; the decrease in the row values is logical if comparing the mean values of a background in figure 4.5a (p. 23) which similarly show that the bottom of the image is less bright. The first 60 columns are left out because they show the very bright reflection of an aluminium frame.

about 1.4.

If a region only meets the requirement of size and area but not those concerning the shape, it is marked as a so called *area* and it coordinates are saved as well. It will be referred to as *area* to avoid confusion with the property equivalent to the number of pixels. The necessity of saving and the usage of this information for further processing is discussed in Section 4.6 (p. 31). In short, it is useful for tracking particles and evaluating the density in the experiment. The information about both balls and *areas* is stored for further processing in consecutive steps.

4.5.1. Treating of Large Regions

Regions featuring large areas greater than the maximum area allowed hint towards three different situations. First of all, it could be balls with different depths overlapping in the image and therefore forming a large area in the binary image. Secondly, some balls are physically detached but the grey value between them is high as depicted in Figure 4.7 (p. 26). The last option for example includes problems with a slim margin on the upper margin of the image where the background might be just above the threshold value of the binarisation, thus, resulting in a slim region of the background being marked as not belonging to the background. All regions larger than half the maximum area, and with greater width and height are passed to another function which handles subimages of the original image. The test for the

maximum grey value, however, prevents that the mentioned slim white margin from being passed on to the function.

A subimage is a rectangular submatrix specified by the bounding box of the area. Two reasons hint towards using only a part of the image. Most importantly, the more erosion is carried out, the more is the precision of the COM is affected by the fact that almost no ball is depicted as a perfect circle in the binary image. Secondly, the time to compute further erosion on the remaining image is not necessary. It can be, depending on the total number of regions, in the range of some tenth of a second, thus, adding up to a considerable amount of time over the course of hundreds of images.

This routine performs further erosion steps in order to separate particles with two different structure elements. First, a large structure element is used where the size is based on the size of the subimage, but restricted to a radius of 30. This is still considerably larger than the one used for the consecutive step with the same element as the erosion of the entire image (radius 6), illustrated in Figure 4.9 (p. 28). The first step is meant to isolate particles, whereas the second is an attempt to minimise the effect of remaining parts of a ball only partially included in the subimage. In figure, the arm shaped part of the area decreased relatively stronger than the convex centre of the lower ball. As a consequence at least the position of the *area* is improved.

4.6. Evaluating Velocity Vectors

The goal of the routine dealing with the evaluation of velocity vectors is to find physically identical balls in consecutive images. In the context of the program, a velocity vector consists of two balls and their positions defining an absolute movement of the particle. In order to find pairs, this routine uses the available information about the position of balls and *areas* of the actual image and the one preceding it. If both images yielded at least one ball, the search for a connection is initiated. Looping through the arrays containing the balls, the algorithm calculates the distance d between the balls. This combination is saved for later consideration if the distance d satisfies:

$$d \leq r_s = 0.8 \cdot d_{ball,\ max},$$

where $d_{max,\ ball} = 245\,\text{px}$ is the maximal ball diameter and r_s specifies the search radius.

For pairs of balls with a distance between one and two times the search radius ($d \in [r_s, 2r_s]$), it is further tested whether old balls or old *areas* lie within the range of one search radius before these pairs are saved. Any greater distance between two particles is omitted. This is justifiable because even the largest appearing balls are not observed to be fast enough to cover a distance greater than the upper limit of the implementation: Consider a ball of maximal size at the front of the acrylic glass box with a diameter of over 240 pixel. I order to cover this distance an absolute velocity of roughly 8 m/s is necessary. A ball moving at the back of the box would even need a velocity exceeding 10 m/s. In the experiment, such high velocities were not observed which is discussed in Section 5.3 (p. 51). However, this could not be known beforehand which is why all velocities greater than one search radius were tracked during implementation of the image processing. Manually checking the images revealed that all velocities above about 6 m/s detected in a false manner.

All pairs of particles stored in a array are tested for double entries and in case the closer, i.e. slower vector is chosen. Double entries occur especially if balls are passing each other closely.

The remaining vectors are stored with positions of the balls, the absolute movements and velocity, the four values for width and height for further analysis. The width and height are important to convert the absolute movement d_{abs} given in px to a velocity v in $\text{m}\,\text{s}^{-1}$ because the diameter of the ball is known to be $d_{ball} = 40\,\text{mm}$ so that the movement can be scaled as follows:

$$v = \frac{d_{abs} \cdot 40\,\text{mm}}{d_{image\ processing} \cdot 8\,\text{ms/image}}, \tag{4.2}$$

where $d_{image\ processing}$ specifies the diameter returned by image processing. Moreover, the image number is identified to allow for manual checking of the data produced by the algorithm. An example of one velocity vector in a data file is shown in Table 4.4 (p. 42).

4.7. Exemplary Entering of a Ball

In this Section, the movement of a ball into the image is shown to exemplify the stages of the image processing. In the first frame shown in Figure 4.11, the focus

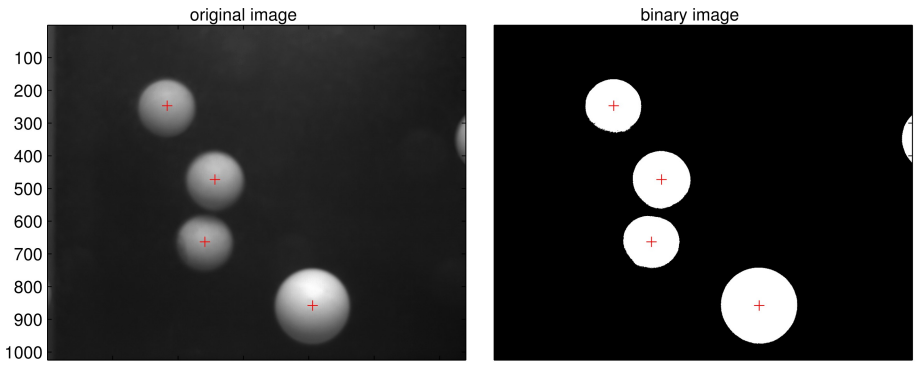

Figure 4.11.: Frame 1: In this frame, a ball begins entering the viewed area at the right margin (at $\approx 350\,\text{px}$ height) and is visible as a thin and high white slice in the binary image.

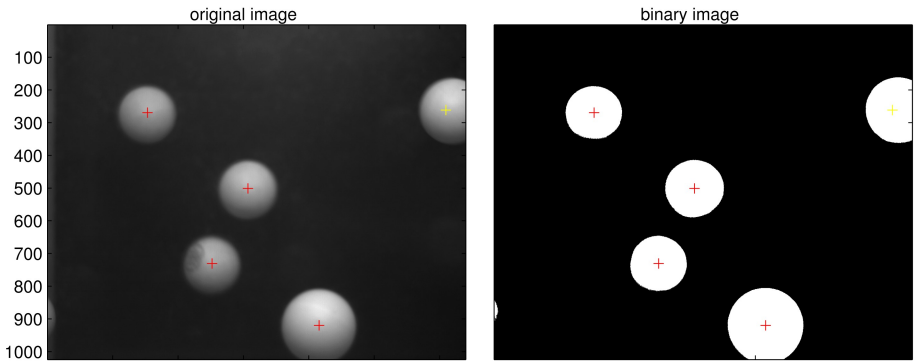

Figure 4.12.: Frame 3: In this frame, the ball is first recognised as an *area* marked with a yellow cross.

lies on the ball that is entering the frame's right border as thin slice. Whereas the other four balls are detected as particles, the rightmost one features a too small area and width and the width height ratio is not close to 1.

In the third frame, depicted in Figure 4.12, the ball has the status of an *area*. Its area accounts to just above the required minimal area but the ratio and width still forbid its detection as a ball until frame 4 (Figure 4.13). However, the area status means it is included in detection of balls density calculations.

In the consecutive frame 4, the ball is detected as a particle with a width-height-ratio of $215/210 = 1.027$. The exact data produced by the image processing program is shown in Table 4.1.

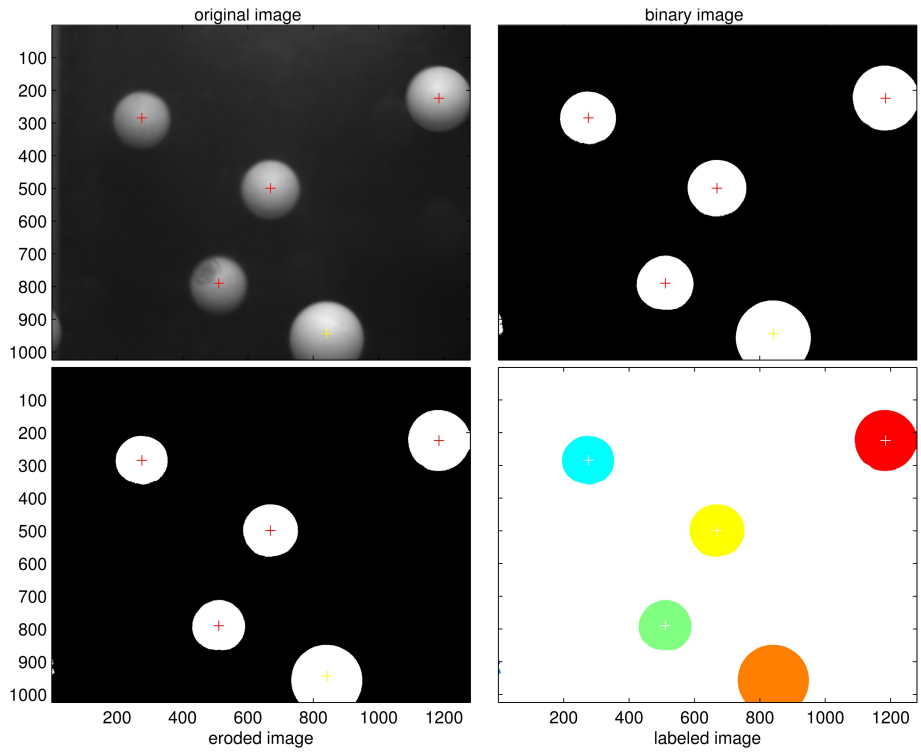

Figure 4.13.: Frame 4: In this frame, the ball is first recognised as a ball. Here, the entire output from the visual debugging of the image processing program is shown with original, binary, eroded and labelled image.

frame	x	y	area	width	height	ratio
1	1270	348	2372	27	130	4.81
2	1244	307	12769	110	178	1.61
3	1219	262	21836	137	189	1.37
4	1185	224	27787	215	210	1.03

Table 4.1.: Data produced for the discussed ball by the image processing program. The minimal area amounts to 12661. All data except ratio in pixels.

4.8. Subimage handling

In this section, the exemplary processing of a subimage is discussed. As explained in Section 4.5.1 (p. 30) the image processing program calls a subimage routine when a large region of white pixels is detected, but its shape is not likely a single ball. This is the case in the original image in Figure 4.14 where one ball is placed slightly before another. The subimage does not include the entire left ball because a first erosion step already took place. A hole in the right ball in the binary subimage is visible caused by erosion around two black pixels inside the ball's region; these are probably due to noise in the camera signal since the rest of the ball's interior region is evenly white. The brand sign is likely to cause the jagged edge of the left ball.

The structure element used to erode the subimage based on the subimage's size has a radius of 21 px. Here, the erosion process is successful in separating the two balls and detecting one as a ball and the other as an *area*. However, the loss of the ball's region is quite high, its shape is not very circular, and it is surprising that the center of mass detection still yields such a good result.

4.9. Error of Image Processing Procedure

4.9.1. Error of Distance

The error of distance was measured by examining the distance given by the image processing between two balls glued to a piece of metal. The metal piece was precisely measured using a micrometre screw to (17.85 ± 0.01) mm. Two balls were then glued onto the surface of the metal using a metal profile to ensure their alignment was perpendicular to the plane defined by the metal surface between them. At first, the front of the metal pointing towards the camera was painted with black ink. However, the front surface is rough and some small uncovered parts remained which reflect the light more intensively than the balls. This causes undesired output of the image processing and, thus, the front surface was covered with black paper.

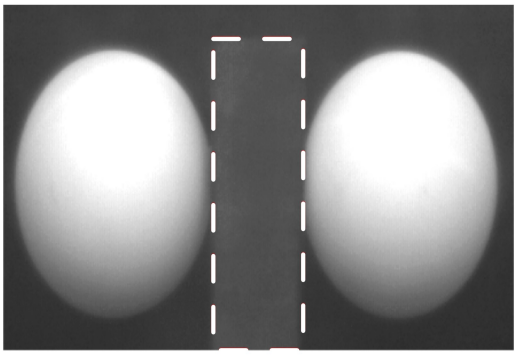

Figure 4.15.: Two balls glued to a precisely measured metal block.

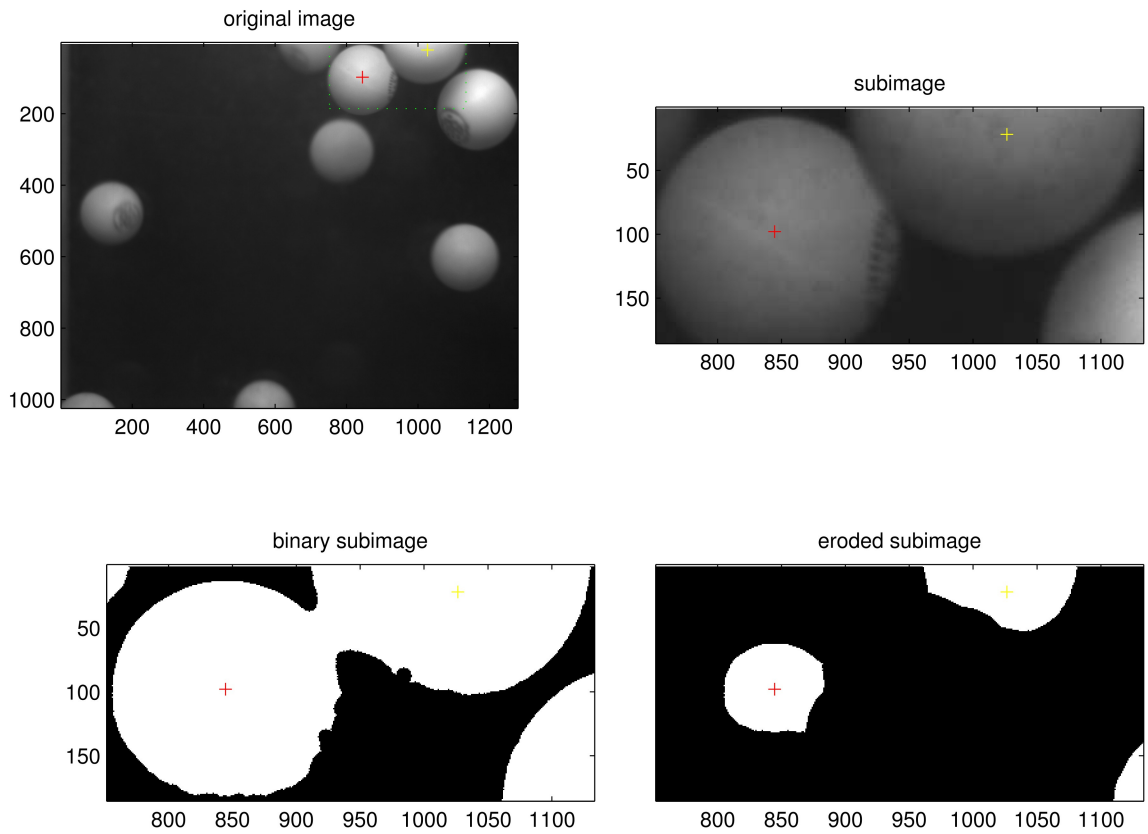

Figure 4.14.: The thin dotted line in the original image indicates the border of the subimage. Only the ball detected in the subimage is also indicated in the original image.

This construction is placed in different positions inside the acrylic glass box and aligned towards the camera. Precise alignment is necessary because even slight rotations can cause a shadow to negatively impact the circled shape of the ball in the binary image thereby affecting the COM-result.

Nevertheless, this method can not detect systematic errors which e.g. result in a constant shift of all positions calculated by the algorithm. For the precision of velocimetry calculations, however, the distance or difference of positions is relevant. Another motivation for this measurement was to find out if the entire setup, including optical and computational parts, showed the same error for every position or whether any irregularities are present e.g. in distant or margin positions of the acrylic glass box. The mean value d_{exp} of the data shown in Table B.2 (p. 79) accounts to:

$$d_{exp} = (17.63 \pm 0.86)\,\mathrm{mm}$$

This converts (using the mean diameter of the data) to a difference of only (1 ± 4) px. However, the value achieved with this measurement is rather an indication of how precise the image processing procedure can be under ideal conditions. For example, any systematic error equally applying to both attached balls vanishes using this method. Furthermore, the balls do not move; their borders are sharper which positively impacts the binarisation and computation of the COM. Therefore this value can be regarded as a lower bound for the expected error, or as a limit of accuracy.

4.9.2. Error of Absolute Position

To evaluate the precision of the the image processing, a sample of 13 images including a total of 46 balls (identified as such by the image processing) were randomly selected. All positions of balls were manually measured using an image viewing program. This included zooming into the ball's section of the image and selecting a rectangle around the ball. Retrieving both upper left corner coordinates and width and height is more precise than pointing to the centre. Some balls are not completely visible in the picture and in this case the width or height information was replaced with whatever was totally visible.

The error was then calculated assuming the manually measured positions to be precise. It has to be noticed, however, that it is, in some, cases difficult to judge where exactly the border of the ball is positioned. Depending on the image a tol-

error σ	x	y	width	height	|x|	|y|	|width|	|height|	distance
mean	0	6	-0.5	3	3	6	3	4	8
std. dev.	9	8	3	4	8	8	2	3	11

Table 4.2.: Difference between the image processing output and manually measured positions and width and heights. All data is given in pixels. The values were computed based on the data in B.3 (p. 80).

erance of one or two pixels could be assumed. Alternatively, balls could have been placed in known positions inside the acrylic glass box in order to fix their position with higher precision. Nevertheless, this was neglected because of two reasons. On the one hand, the effort to fix and determine balls on exact positions would require more experimental set up to hold them. Second of all, the experiment is deals with moving balls and the image sharpness would unrealistically improved if only considering fixed particles.

For the four parameters x- and y-coordinate and width and height differences in both directions, positive and negative, were observed. The mean of the error for x, called σ_x, for example, computes to zero. Therefore, it is also interesting to calculate the mean of the absolute value of the difference of the program output and manual measuring. All means are given in Table 4.2 and the complete data can be found in Table B.3.

As noted above, the mean x error σ_x diminishes, yet $\sigma_{|x|} \approx 3\,\text{px}$. This means that the accuracy in x-direction is roughly 3 px but overall the image processing procedure does not favour left or right drift. However, because most balls remain in the view of the camera only over the course of few images, it is most likely that the error will not average to a value close to zero. Thus, for the evaluation of the error of a velocity $\sigma_{|x|}$ should be considered.

On the contrary, the values of both σ_y and $\sigma_{|y|}$ are identical in magnitude. This implies that the image processing program generally estimates the y-coordinate of the balls roughly 6 px to high. In fact, only one value for Δy is negative. Bearing in mind the decrease of overall luminosity of the images from top to bottom as discussed in Section 4.2 (p. 21), it seems consistent that the error in y-direction is rather systematic. The reason for the high standard deviation of σ_y and $\sigma_{|y|}$ lies in the inclusion of two outliers (Δy=49.9 px and Δy=28.9 px). Without them, the standard deviation decreases to roughly 3 px as compared to 8 px before. All outliers are included in the calculation in this section because the focus lies on finding the

accuracy of a random sample.

Not unlike σ_x and $\sigma_{|x|}$, the width's error nearly evens out but the absolute error $\sigma_{|width|}$ remains. Here, however, the variance is smaller. The height was overrated, i.e. Δheight< 0, in all but nine cases, whereas the width seems equally over- and underrated by the algorithm. This is important for the calculation of velocity vectors since the estimated radius (mean of width and height) is used to scale the absolute movement to a velocity in $\mathrm{m\,s^{-1}}$ as shown in Equation (4.2) (p. 32).

4.9.3. Error of Velocities

Whereas the accuracy of the position is solely governed by the error in x- and y coordinates, the velocity calculation also relies on the correct determination of the diameter d_{IP} by the image processing. Equation (4.2) (p. 32) shows this impact. The calculation of the x-component v_x of an velocity reads:

$$v_x = \frac{\Delta x \cdot 40\,\mathrm{mm}}{d_{IP} \cdot 8\,\mathrm{ms/image}} = \frac{\Delta x}{d_{IP}} \cdot f_{conv.}$$

with a conversion factor $f_{conv.} := 5\,\mathrm{m\,s^{-1}}$ since Δx correctly bears the dimension px/image. The Gauss error law for the evaluation of a velocity's error σ_{v_x} yields:

$$\begin{aligned}\sigma_{v_x}^2 &= (\sigma_{\Delta x} \cdot \partial_{\Delta x} v_x)^2 + (\sigma_{d_{IP}} \cdot \partial_{d_{IP}} v_x)^2 \\ &= \left(\sigma_{\Delta x} \cdot \frac{f_{conv.}}{d_{IP}}\right)^2 + \left(\sigma_{d_{IP}} \cdot \frac{\Delta x \cdot f_{conv.}}{d_{IP}^2}\right)^2\end{aligned}$$

The error σ_{v_y} has an analogous form and leads to the error of a velocity $v = \sqrt{v_x^2 + v_y^2}$ named σ_v:

$$\begin{aligned}\sigma_v^2 &= (\sigma_{v_x} \cdot \partial_{v_x} v)^2 + (\sigma_{v_y} \cdot \partial_{v_y} v)^2 \\ &= \left(\sigma_{v_x} \cdot \frac{v_x}{v}\right)^2 + \left(\sigma_{v_x} \cdot \frac{v_x}{v}\right)^2 \\ \Rightarrow \sigma_v &= \frac{\sigma_{v_x} \cdot v_x + \sigma_{v_y} \cdot v_y}{v}\end{aligned} \tag{4.3}$$

In the previous section, Section 4.9.2 (p. 37), it was discussed that the absolute errors are a better choice because one ball's trajectory has too few points in order to average out the statistic error. Likewise, it is better to assume the maximum of the absolute width and height error as the error of the diameter d_{IP}. This yields

$\sigma_{\Delta x}$	$\sigma_{\Delta y}$	$\sigma_{d_{IP}}$
3	6	4

Table 4.3.: Values [px] used to determine a velocity's error.

the values given in Table 4.3. Therefore, σ_{v_x} and σ_{v_y} become:

$$\begin{aligned} \sigma_{v_x} &= \sqrt{\left(\frac{15}{d_{IP}}\right) + \left(\frac{20 \cdot \Delta x}{d_{IP}^2}\right)^2}\,\mathrm{m\,s^{-1}} \\ \sigma_{v_y} &= \sqrt{\left(\frac{30}{d_{IP}}\right) + \left(\frac{20 \cdot \Delta y}{d_{IP}^2}\right)^2}\,\mathrm{m\,s^{-1}} \end{aligned} \tag{4.4}$$

To get an idea of the magnitude of the error a ball with relatively small $d_{IP} = 175\,\mathrm{px}$ and high $\Delta x = 48\,\mathrm{px}$ and $\Delta y = 166\,\mathrm{px}$ is considered. This represents a situation were the error should be rather high because the ball is fast but at the back of the container (smaller denominator): σ_{v_x} =0.09 $\mathrm{m\,s^{-1}}$, σ_{v_x} =0.19 $\mathrm{m\,s^{-1}}$ and σ_v =0.04 $\mathrm{m\,s^{-1}}$.

4.10. Box Counting

Having obtained the velocity data from the image processing program, it is possible to further analyse the physical properties of the observed particles. An example of one line of data is given in Table 4.4. The image processing usually analyses 7×817 images for each combination of ground plate and acceleration. In turn, this yields thousands[1] of lines of data, and together they make up one *sample*.

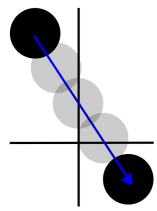

Figure 4.16.

For some of the results given in this Chapter, the analysis of the data is based on dividing the image into small boxes like posting a grid or net on the image. The used 15 by 12 grid is visualised in figure 4.17. The reason for choosing the scale for the grid lie in the practical thought that too few boxes might hinder the visualisation of data. On the other hand, a too fine grid yields few data points lying in each box and makes it difficult to attain good statistical results. The image dimension of $1280 \times 1024\,\mathrm{px}$ causes the boxes of the chosen grid to be quadratic with a equal

[1]Depending on the combination, between 5000 and 12000 vectors might be found.

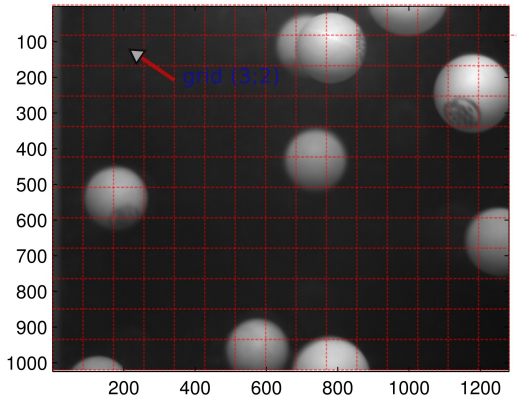

Figure 4.17.: 15 by 12 grid with upper left corner as position (0;0).

width and height of 85 px. The data is assigned to the boxes using the coordinates of the detected balls. Therefore, a single particle is always attached to one box and a single velocity can be part of at most two boxes.

For fast particles or particles at a corner of a box, this raises the problem that more than two boxes might be included in the ball's path as visualised in Figure 4.16. The balls at the front have the highest potential to do so, because they appear larger. Consider a ball at the front of the window with a diameter of roughly 240 px and a velocity of $3\,\mathrm{m\,s^{-1}} \approx 144\,\mathrm{px/frame}$. One box has a width/height of 85 px so this ball has the chance to trick the data analysis by covering more than an entire box. It is important to notice that the absolute movement consist of a two components for x and y direction. For the problem of crossed boxes, the pixel movement in one direction has to be considered. However, only a small amount of velocity data features such a high pixel movement in one direction. Generally the pixel movement decreases in z direction. For example a ball with diameter of 170 px equivalent to 40 mm at a velocity of $3\,\mathrm{m\,s^{-1}}$ shows an absolute pixel movement of roughly 100 px. The problem of balls covering the edge of a box, however, remains. An advantage of the relatively small grid is that such an assignments is not accounted for too far away.

On the other hand, triple entries would introduce the need for a weighting of positions. If one ball has exactly one position per image, the particle density does not have to be weighted. If, however, more than one position or grid box is possible, the calculation would necessarily need a weighting factor in order to prevent an overweighting of those particles.

x_1	y_1	x_2	y_2	$\|v\|$	v_x	v_y	h_1	w_1	d_1	h_2	w_2	d_2	file	#
505	943	497	857	87	-8.8	8.7	205	209	207	206	202	204	2	42

Table 4.4.: An example of a velocity vector with all information produced by the image processing. Thousands of such lines of data make up one *sample*. Here, the values are presented in a rounded form although the COM might results in subpixel accuracy, like $x_1 = 505.407\,33\,\text{px}$. However, this should not tempt to think that the position is measured with such precision. The terms w_1, h_1, d_1 indicate the width, height and diameter of the first ball with position $(x_1; y_1)$. The second ball is analogous. The term "file"$\in [1; 7]$ stands for the image file consisting of 817 image-frames indicated by "#"$\in [1; 817]$. All data is given in px, except the image file and number.

5. Results

5.1. Statistical Validity

Normally, one would expect that the sum of all velocity vectors over a sample I of data would add up to a value close to zero because all directions should be equally present:

$$\begin{aligned} &\sum_{i \in I} \vec{v}_i \approx \vec{0}, \text{ or} \\ &\|\sum_{i \in I} \vec{v}_i\| \approx 0 \end{aligned} \tag{5.1}$$

This would particularly be expected if the images used to calculate the data of I would be taken of the the entire box. However, the images are sections of the acrylic glass box. Moreover, overlaying balls cause loss or false detection. Table 5.1 reveals that all samples do not hold the condition of Equation (5.1). In fact, nearly all samples listed show very large summarised values.

Nevertheless the mean $\langle v \rangle$ should be approaching zero. This is the case for all data samples as the values in Table 5.1 show. The fact that all but four of the summarised values and $\langle v_{x,y} \rangle$ are negative is most striking. Therefore, the observed balls are moving left and down, however, the magnitude of the mean determines the overall magnitude of this effect; the order of the overall movement is negligible. As an example, the evolution of the mean of one position and ground plate over the course of all included vectors is shown; in Figure 5.1, the data collected using the large structure ground plate in the border position is displayed. Approximately 1000 vectors are needed to reduce the means $\langle v_{x,y} \rangle$ to roughly $0.1\,\mathrm{m\,s^{-1}}$. Including more then 5000 vectors does not seem to change the order of the resulting mean value significantly. The sample size is above 10000 for all but the two lower accelerations of the small structured ground plate. Thus, the chosen sample size appears to be sufficient to ensure the results are not affected by statistic deviation.

sample	a [g]	$\sum v_x$ [m s^{-1}]	$\sum v_y$ [m s^{-1}]	$\langle v_x \rangle$ [m s^{-1}]	$\langle v_y \rangle$ [m s^{-1}]
central, large	4.6	-209	-448	-0.02	-0.04
	6.0	-109	-313	-0.01	-0.03
	7.6	-509	-587	-0.05	-0.06
	8.2	-380	-863	-0.04	-0.1
border, large	4.6	71	-265	0.005	-0.02
	6.0	-379	-253	-0.03	-0.02
	7.6	-435	-465	-0.03	-0.04
	8.2	-408	-362	-0.03	-0.03
central, small	4.6	-48	-280	-0.01	-0.06
	6.0	44	-232	0.01	-0.03
	7.6	164	-8	0.02	-0.001
	8.2	128	4	0.01	0.0004
border, small	4.6	-95	-184	-0.02	-0.04
	6.0	-81	-472	-0.01	-0.04
	7.6	-364	-393	-0.03	-0.03
	8.2	-344	-385	-0.03	-0.04

Table 5.1.: Statistical data for all samples used. Sums $\sum v_{x,y}$ are rounded to integers and the means $\langle v_{x,y} \rangle$ are rounded to the first non-zero digit. One sample usually consist of the analysis of 7×817 images which usually relates to at least 11000 velocity vectors.

5.2. Particle Density

The particle density is a good starting point for the investigation of the granular gas made of table tennis ball because it can also point to problems with the image processing steps if the density distribution shows significant, yet unexplainable, trends. The density distribution also answers the question to which extend the processed data, e.g. a mean, of a specific area is expected to be similar to one calculated in another area of the grid.

The data required for the calculation of the particle density is given as a count of particles in one box of the grid. This value has to be converted to a useful unit. Here, the density d was evaluated as the count of particles in a virtual $10 \times 10 \times 10$ cm cube because the length scales of the balls would allow to envision the density specified by a certain value. Of course, corrections for the size of a grid box and the total number of images analysed have to be made:

$$d = \frac{\#in\ box}{\#images} \cdot f_{geometry},$$

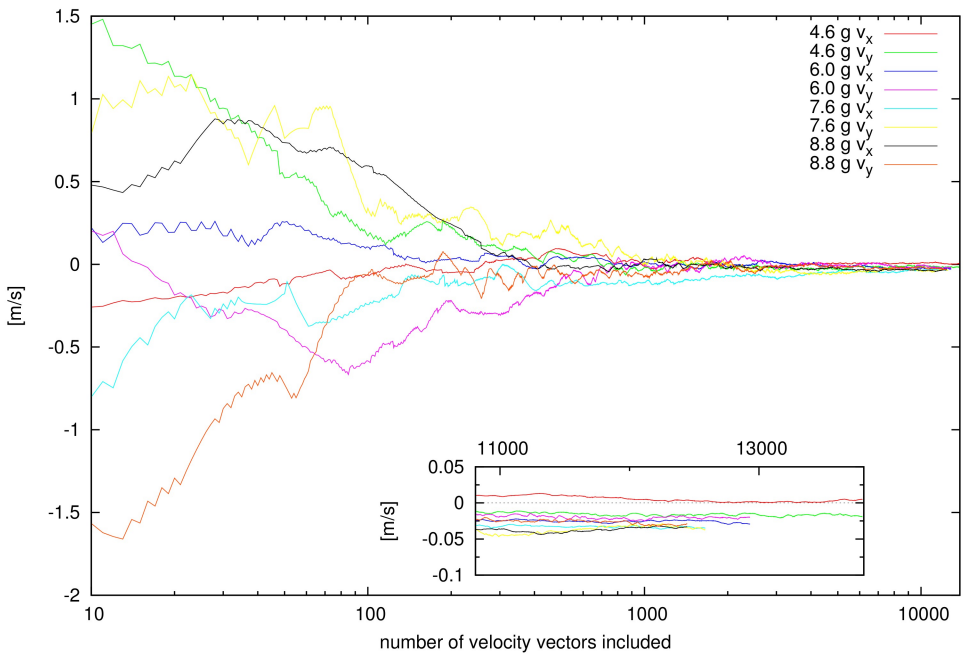

Figure 5.1.: The mean of both components $\langle v_{x,y} \rangle$ of the data collected using the large structured ground plate in a border position approaches zero, the more vectors are included.

where $\#in\ box$ is the total number of particles in the grid box, $\#images$ represents the number of images and $f_{geometry}$ is a conversion factor from the volume of a grid box $v_{grid\ box}$ =85 × 85 × 305 mm to the virtual 10 × 10 × 10 cm cube. However, $v_{grid\ box}$ remains an approximation because of the angle of beam, i.e. the area inside the one grid element is slightly larger at the back of the acrylic glass box.

The equilibrium density, i.e. all balls are evenly distributed within the acrylic glass box, computes to:

$$d_{equi} = \frac{\#balls}{v_{box}} \approx 0.18\,\text{balls}/10\text{cm}^3 \tag{5.2}$$

for 12 balls. In the density plots, it is indicated by a dashed line. To handle the amount of numbers in the 15 by 12 grid, the values in the plots are either the sum of all values in one row of the grid (left part of plots), or the sum of the values in one column of the grid (right part of the plot). Thus, the density in x- and y-direction can be analysed. Because one grid element is smaller than most ball's diameter the amount of particles detected in a one grid box wide margin is very low. Therefore, this margin is not included in the plots is this section as it does not bear any physical

meaning. An example of the entire observed data is given in Figure A.1 (p. 74).

The central view with the large structure ground plate yields the data in Figure 5.2. The density in horizontal direction is quite constant whereas the density in vertical direction decreases slightly. This effect is slightly stronger for lower accelerations. The fact that the density is clearly above the equilibrium density, indicates that the shaking is not sufficient to spread the balls evenly. Fewer balls are registered in the top part of the container.

This plot shall be compared to the results of the smaller ground plate in Figure 5.3 which shows differing values. Here, the shaking acceleration seems to be the main factor determining the vertical trend of the density. It appears that for the small structured ground plate only the highest acceleration excites the balls into a state where the overall vertical density only decreases slightly. Especially the data for accelerations 4.6 g and 6 g display a significant decrease in density above a certain height. Almost no particles were observed above half the height of the container (270 mm) when shaking with the lowest amplitude. Surprisingly, the overall vertical density is higher for an acceleration of 8.8 g using the small than the large structured ground plate. The overall horizontal density is well below the equilibrium value for the lowest amplitude which is logical considering only few particles are detected in the top half of the container. Therefore, the overall density in horizontal direction increases with the shaking amplitude. However, unlike the lowest amplitude, the other three show a rise in density on the right border. The highest acceleration (8.8 g) seems to have a comparable rise on the left border as well, yet these trends are minimal.

The horizontal density in the border position shows a increase at the left margin which represents the physical border of the container. This effect is more striking for the small structured ground plate displayed in Figure 5.5 yet still clearly visible for the data gathered using the large structured ground plate in Figure 5.4 as well. This might be due to balls bouncing off the left acrylic glass window. The continuity of the data from one position to the other of the horizontal data is given for all measurements except for the the highest acceleration (8.8 g) of the small structured ground plate which was computed to a significantly higher value at $x \approx 240$ mm for the central position.

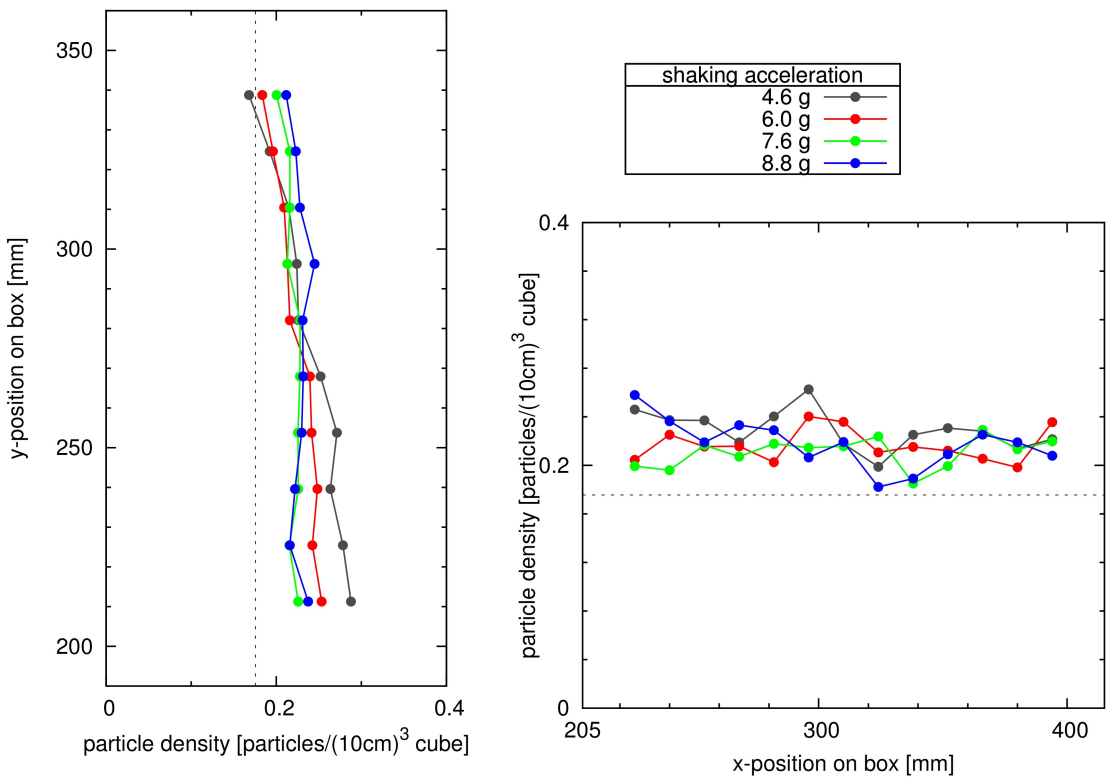

Figure 5.2.: Density of particles with large structured ground plate in central position.

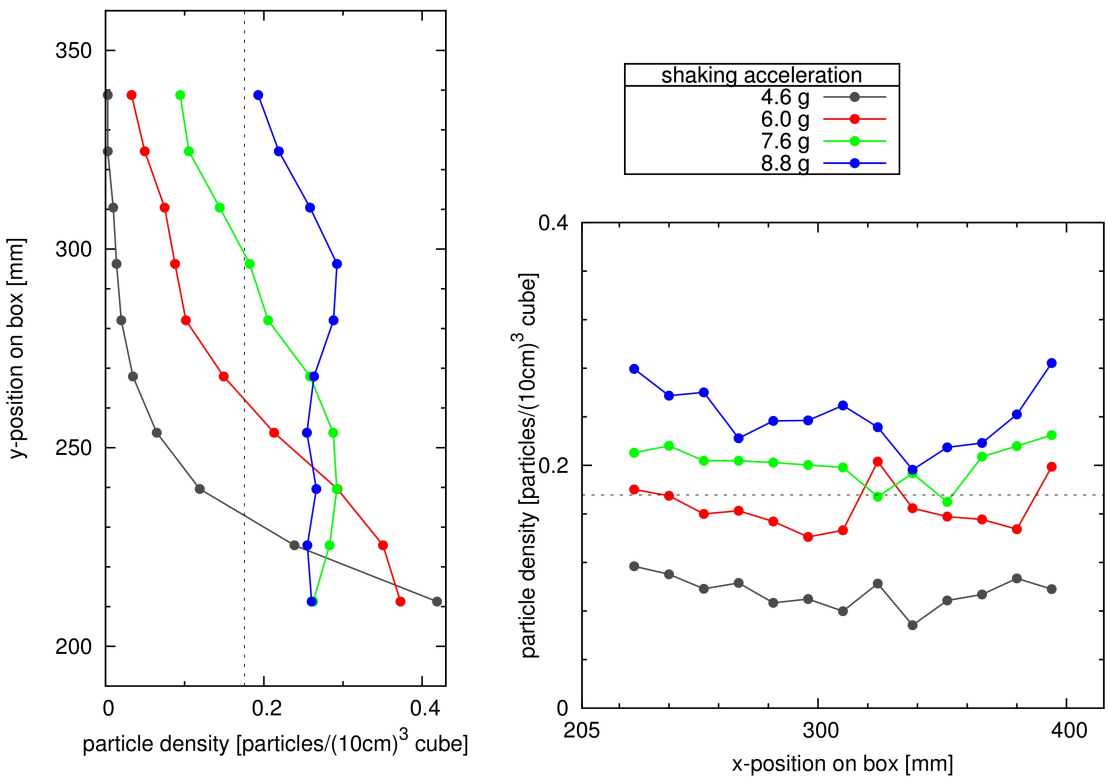

Figure 5.3.: Density of particles with small structured ground plate in central position

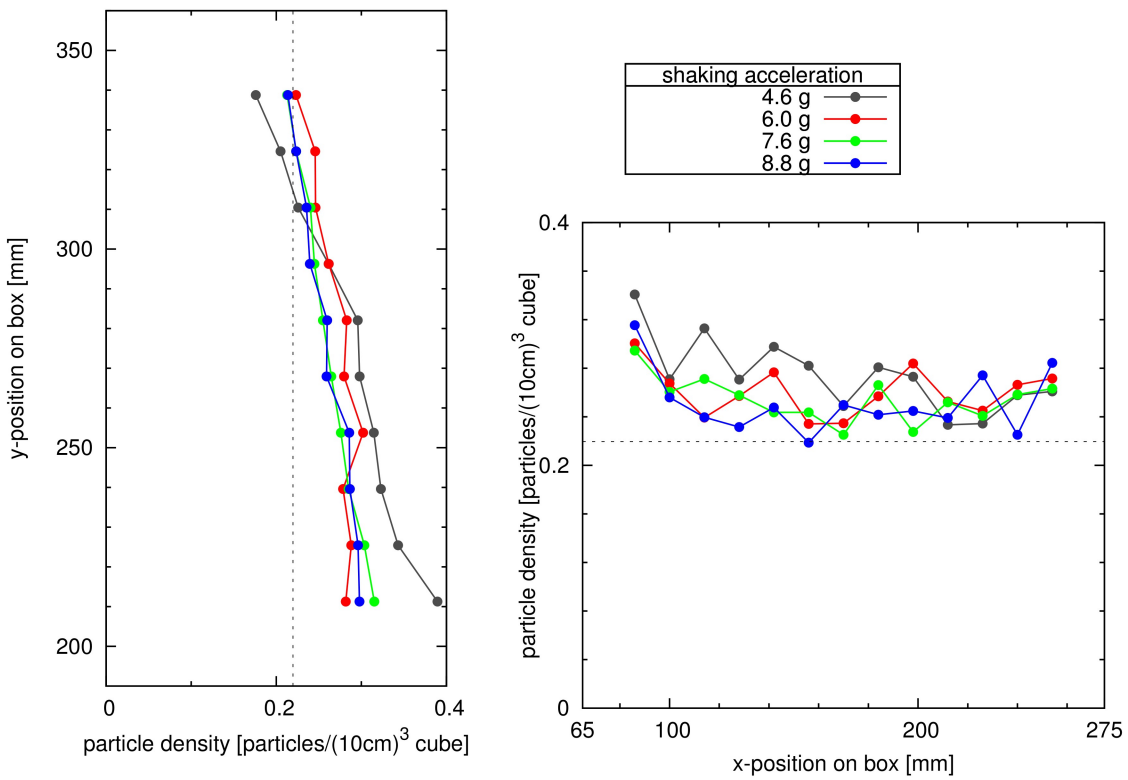

Figure 5.4.: Density of particles with large structured ground plate in border position.

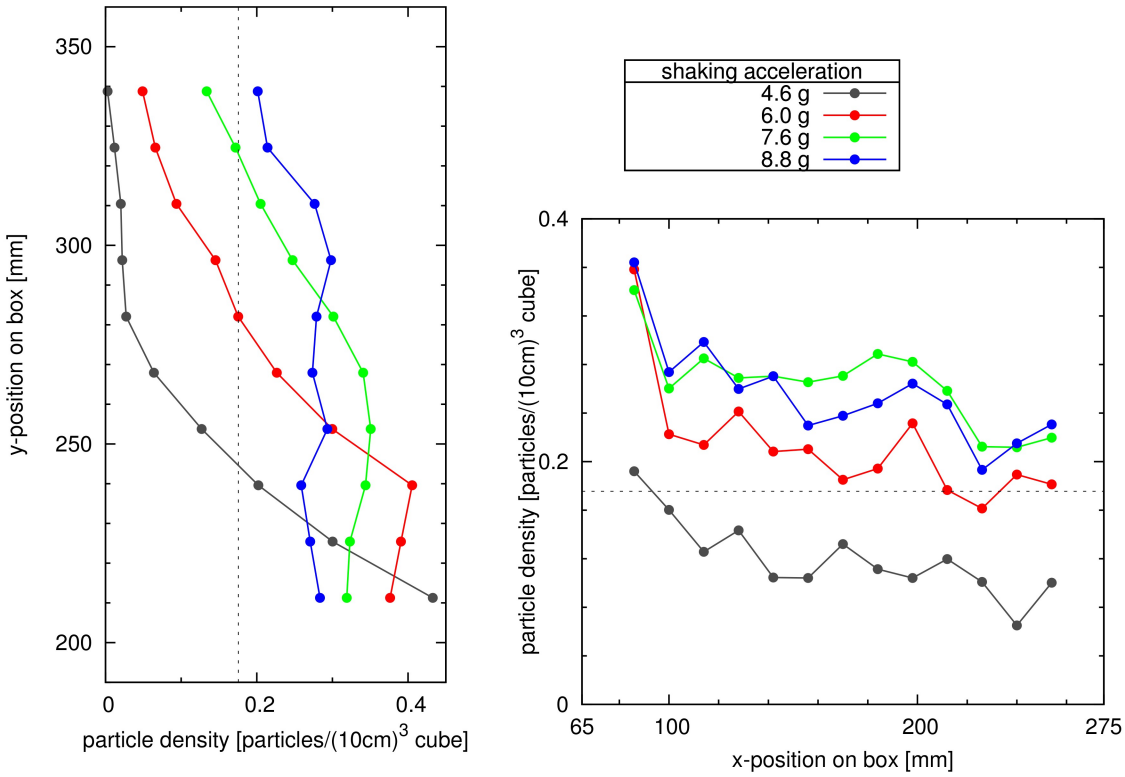

Figure 5.5.: Density of particles with small structured ground plate in border position

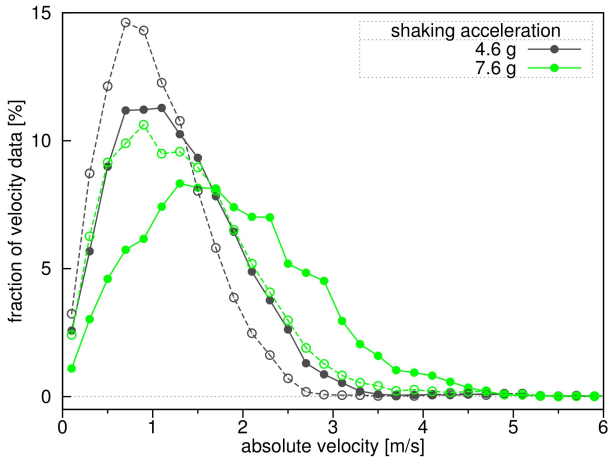

Figure 5.6.: Distribution of the absolute velocity using the large structured ground plate. Solid lines correspond to the central and dashed to the border position. Apparently, the the form of the distribution of the higher acceleration in border position matches the form of the higher acceleration in central position.

5.3. Velocity Distribution

The velocity distribution can be analysed for the absolute velocity $v = |\vec{v}|$ and for the spatial component$|v_x|, |v_y|, |v_z|$ individually. In this section, the absolute velocity $v = |\vec{v}|$ is discussed. If not otherwise stated, v_x actually refers to $|v_x|$ and y- and z-direction analogous. The bin-width of all following plots is $0.2\,\mathrm{m\,s^{-1}}$. Solid lines are referring to the central position and same-coloured dashed lines refer to the same acceleration observed in the border position.

The distribution for the large structured ground plate seems to be not only dependant on the acceleration, but also on the position. For two accelerations, both positions are plotted in Figure 5.6. The data for the border position shows significantly more slower velocities.

As a comparison, the same accelerations for the small structured ground plate are given in Figure 5.7. For the small structured ground plate, no significant difference between the positions is visible. Another difference between the ground plates can be seen by comparing the three highest accelerations. Whereas the distribution for the small structured plate shifts toward higher velocities as expected, few differences are observed with increasing acceleration for the large structured ground plate. This is depicted in Figure 5.8. The reason might lie in the fact that the large ground plate excites the particles not significantly more above 6 g. This is suggested by the little difference in density between the accelerations discussed in Section 5.2 (p. 44)

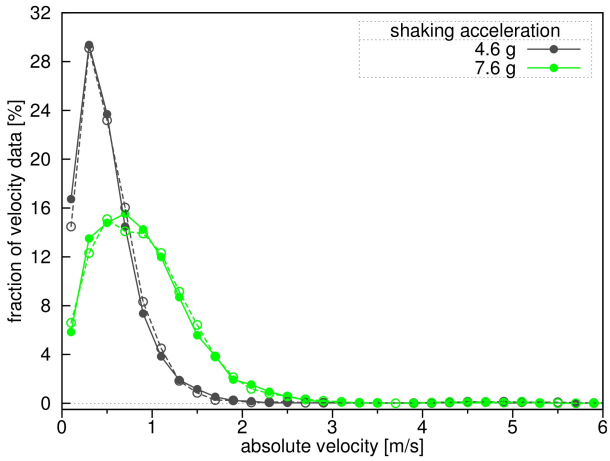

Figure 5.7.: Distribution of the absolute velocity using the small structured ground plate. Solid lines correspond to the central and dashed to the border position. Both distributions are nearly identical.

especially Figure 5.2 (p. 47).

To compare the other accelerations individually the data for each position is given in the appendix in figures A.2 (p. 74) to A.5 (p. 75).

5.3.1. Spatial Velocity Distributions v_x and v_y

The analysis of the spatial velocity, i.e. the components v_x and v_y separately clearly shows that v_y, the vertical component, has significantly less slower data; the overall horizontal movement of balls is slower. This is not surprising because the shaker provides vertical movement. The data for the central position of the small structured ground plate is plotted in Figure 5.9 and the border position's data of the large structured ground plate is depicted in Figure 5.10.

In analogy to the distribution of the vector velocities mentioned in the previous section, the slower velocities take up a considerably higher amount when the small structured ground plate is used. The spatial distribution of the small structured ground plate with the highest acceleration is comparable to the distribution of the large structured ground plate using the lower accelerations. Plots for all four positions and ground plates are included in the appendix in Figure A.6 (p. 76) to A.7.

The horizontal v_x velocities could be impacted by the presence of the left window of the container, however, the distribution is quite symmetric for the small structure ground plate. The plot in Figure 5.11 shows the non-absolute horizontal velocity in

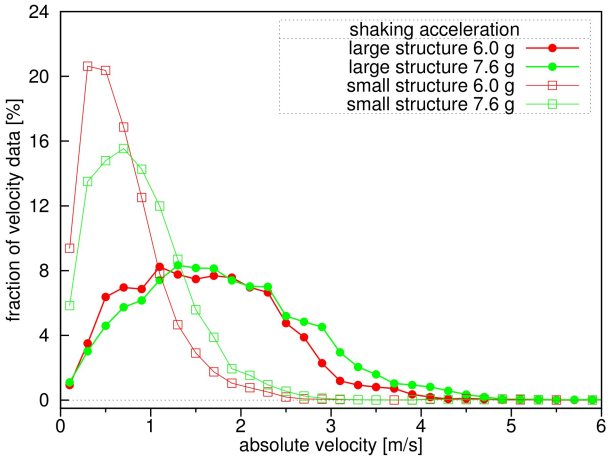

Figure 5.8.: The velocity distribution of the small structured ground plate shifts towards higher velocities with increasing accelerations. This expected difference is less obvious for the large structured ground plate.

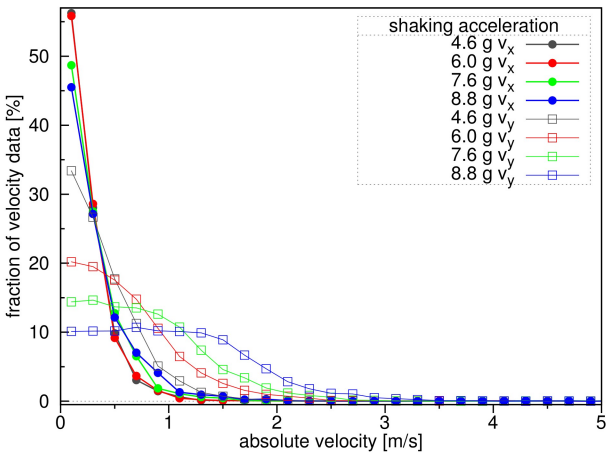

Figure 5.9.: The distribution of the spatial velocities v_x and v_y of the small structured ground plate (central position) show that the vertical movement has a significantly higher overall magnitude.

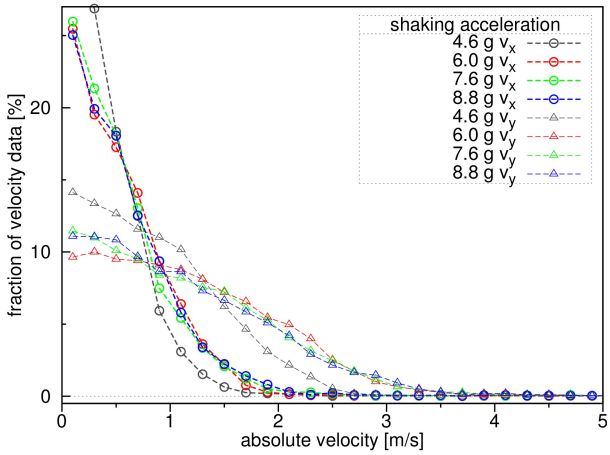

Figure 5.10.: The distribution of the spatial velocities v_x and v_y show that vertical movement has a significantly higher overall magnitude. Data taken with the large structured ground plate in border position.

a 250 px wide margin on the left. Thus, it seems that the bordering window does not affect the absolute horizontal velocity v_x. The large structure ground plate, on the other hand, features a slightly shifted distribution with higher velocities in the direction of the window, yet the effect seems small.

Moreover, the magnitude of the acceleration has a very limited effect on the distribution of the large structured ground plate. Instead, the position is a major factor for this ground plate as the plot for the y-direction in Figure 5.12 reveals. The central position features higher velocities and the for both shown accelerations, and for the highest acceleration, the distribution is less monotonic, and less decreasing than any other distribution.

5.3.2. The Velocity Distribution v_z

The information about the velocity v_z in z-direction is only indirectly gained. Computing the difference of the two ball diameters belonging to one velocity vector yields a difference which can be turned into a movement as well. This distribution is plotted in Figure 5.13 and the majority of the velocities is below $0.5\,\mathrm{m\,s^{-1}}$. The x-component is shown as well because the two directions should be equally distributed according to the symmetric ground plates. The other ground plates and positions qualitatively show the same distribution, however, are left out of the Work because the values can not be explained properly and add no further information.

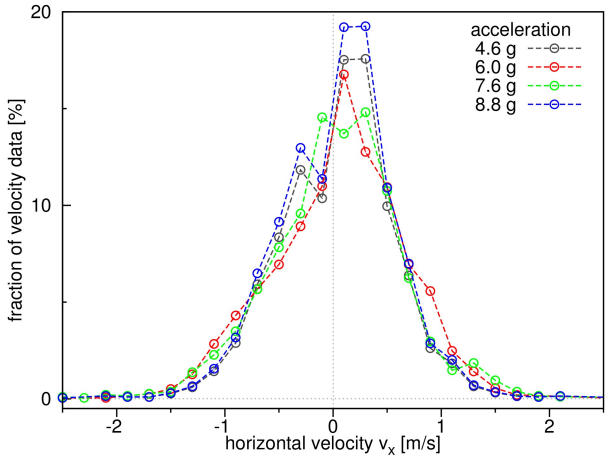

(a) large

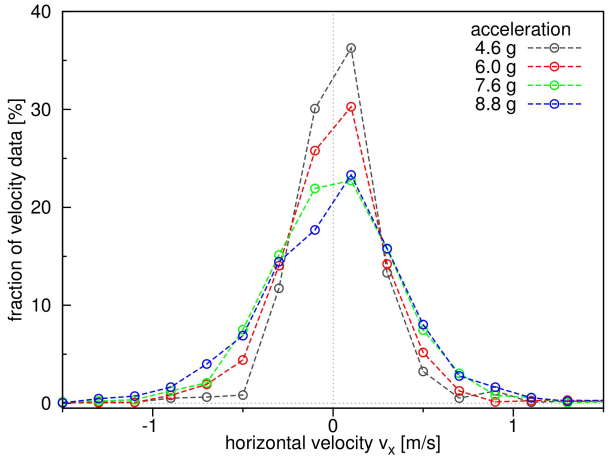

(b) small

Figure 5.11.: The distribution of the non-absolute horizontal velocity v_x for the large structured ground plate (a) shows slightly faster values moving towards the window, whereas the distribution the small structured ground plate (b) seems to be almost symmetric. For all curves, the number of included velocity vectors accounts to roughly 2000, except for the lowest acceleration of the small structured ground plate where only 954 vectors are registered in the 250 px wide margin.

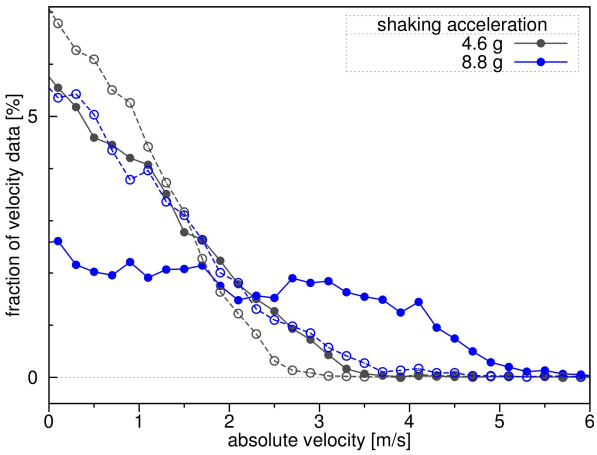

Figure 5.12.: The distribution v_y of the large structured ground plate shows a dependency on the position.

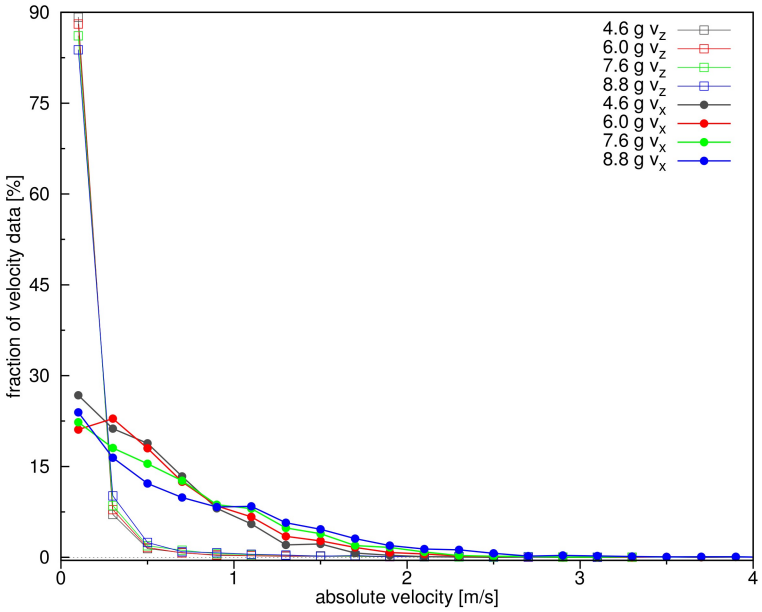

Figure 5.13.: The distribution in z-direction displays almost no velocity higher than roughly $0.5\,\mathrm{m\,s^{-1}}$. The data belongs to the large structured ground plate in central position.

	large structure		small structure	
	center	border	center	border
acceleration [g]	$[\mathrm{m}^2\,\mathrm{s}^{-2}]$			
4.6	2.29	1.63	0.44	0.59
6.0	3.47	2.74	0.77	0.96
7.6	4.51	2.67	1.16	1.34
8.8	6.18	2.68	1.90	2.06

Table 5.2.: The term $\langle v^2 \rangle$ for all measurements of the experiment.

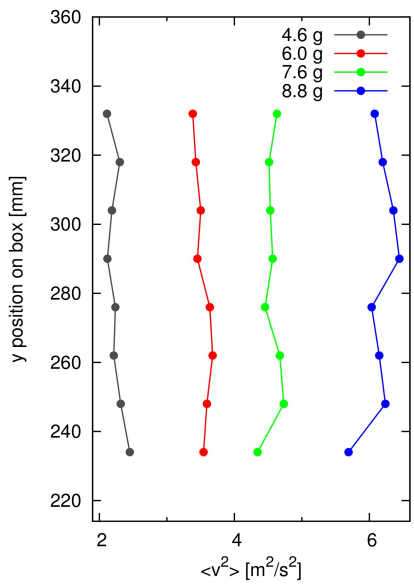

Figure 5.14.: Values of $\langle v^2 \rangle$ computed separately for the rows of the grid.

5.3.3. Temperature and Velocity Distribution

The granular temperature T is proportional to $\langle v^2 \rangle$ as explained in Section 2.1.1 (p. 3). Therefore, the term $\langle v^2 \rangle$ is computed for all samples yielding the results in Table 5.2. The values rise, as expected, with increasing shaking acceleration except for the combination large-border. The large structured ground plate shows higher values which is not a surprise considering the fact that the large structure features considerably more higher velocities as displayed in Figure 5.8 (p. 53).

Moreover, it is possible to fit the distribution functions mentioned in Section 2.1.1 (p. 3) to the velocity distribution data. Beforehand, however, it has to be made sure that the term $\langle v^2 \rangle$ does not vary too much depending on the position on the grid. This is important since the theoretical velocity distribution functions are based on the assumption of a gradient-free gas. From the results gained in Section 5.2 (p. 44)

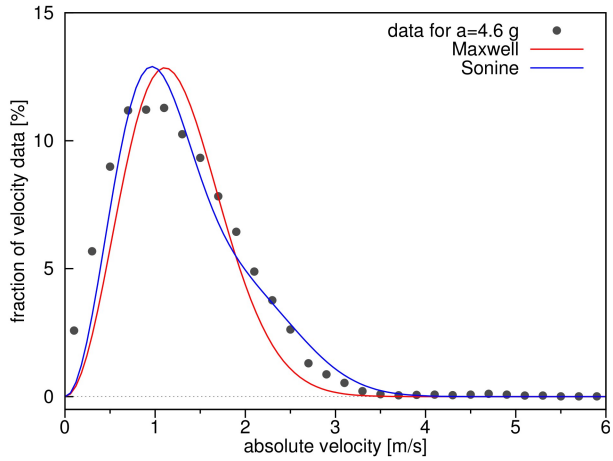

Figure 5.15.: Fit for the data of an acceleration a=4.6 g

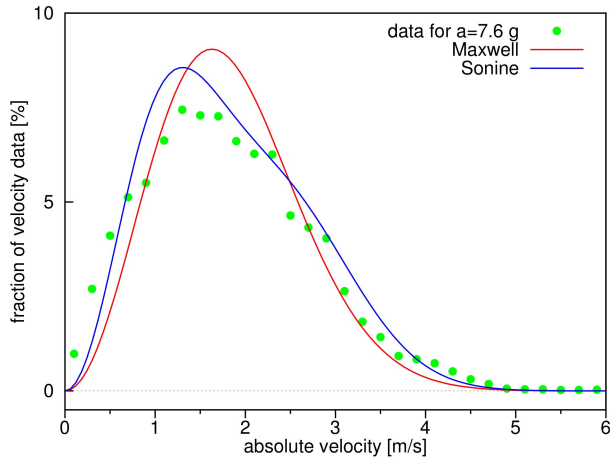

Figure 5.16.: Fit for the data of an acceleration a=7.6 g.

about the density, it is clear that the small structured ground plate does not hold this property for all but the highest acceleration. The density is declining rapidly with rising y-position on the box. This means that few balls are expected in the top part and the high velocities observed are expected in the lower part, thus establishing a gradient in vertical direction. On the other hand, the density data suggest no such gradient for the large structured ground plate. Because the border position shows no significant increase for $\langle v^2 \rangle$ above 6.0 g (see Table 5.2) and the density decreases slightly with height (Figure 5.4 p. 49) the central position is selected for the fit.

The plot in Figure 5.14 shows that the term $\langle v^2 \rangle$ has no striking dependency on the vertical position, thus, the assumption mentioned above might hold. The resulting fits are given in Figure 5.15 for a shaking amplitude of 4.6 g and in Figure 5.16 for 7.6 g

	Maxwell	Sonine	
acceleration [g]	$\langle v^2 \rangle$ [$\mathrm{m^2\,s^{-2}}$]	$\langle v^2 \rangle$ [$\mathrm{m^2\,s^{-2}}$]	a_2
4.6	1.85	1.92	0.18
7.6	3.97	3.02	0.09

Table 5.3.: The fits of figures 5.15 and 5.16 resulted in values for the term $\langle v^2 \rangle$ and the first non trivial Sonine coefficient a_2. The relatively small errors are not given because they overestimate the quality of the plot.

The fit resulted in the parameters given in Table 5.3.

5.4. Flow Field

Flow fields are important to display any form flow or gradient. Figure 5.17 shows an exemplary flow field from the experiment which was normalised so that all vectors have the same length. Adjacent vectors pointing at each other might seem contradictory, however, it has to be noticed that the mean value of such a vector accounts to $0.006\,\mathrm{m\,s^{-1}}$. The maximum in this case is $0.28\,\mathrm{m\,s^{-1}}$, yet this value was recorded in a margin box with very few vectors, thus, being statistically unreliable. The overall impression of all flowfields is that no gradient of flow or convection roll is present. Therefore, only one of these plots is presented.

5.5. Anisotropy of Temperature

The anisotropy $R := \frac{T_{vertical}}{T_{horizontal}} = \frac{T_{ver}}{T_{hor}}$ of the temperature is displayed in Figure 5.18. The error was derived by calculating the standard deviation of the values of R for each of the 7×817 image samples separately. All values are $R > 1$, thus, the vertical component is higher. This is consistent with the visual impression of the plot in Figure 5.6 and the fact that the shaker provides vertical movement.

The value of R remains almost constant for the border position of the large structured ground plate and increases slightly for its central position, however, the increase is not monotonic. With increasing acceleration, the values of R for both positions differ more and the border positions' value is lower for all four data points.

For the small structured ground plate, this is also the case for all but the lowest acceleration, where the values are nearly identical and show the lowest overall value. With increasing shaking acceleration the border value is above the central value and

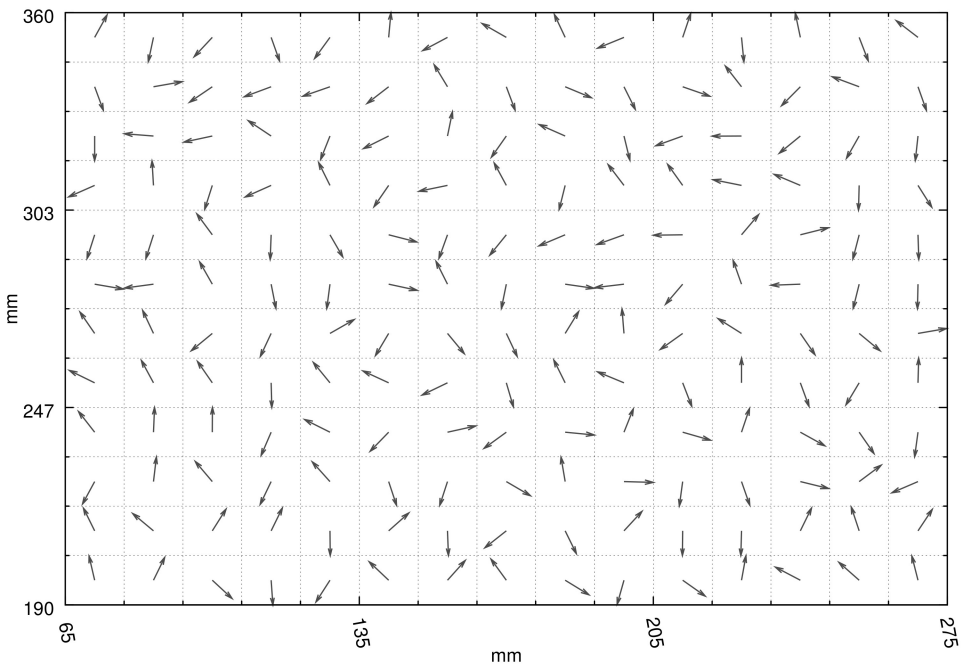

Figure 5.17.: Exemplary normalised flow field using the large structured ground plate in a central position with a shaking acceleration of 8.8 g.

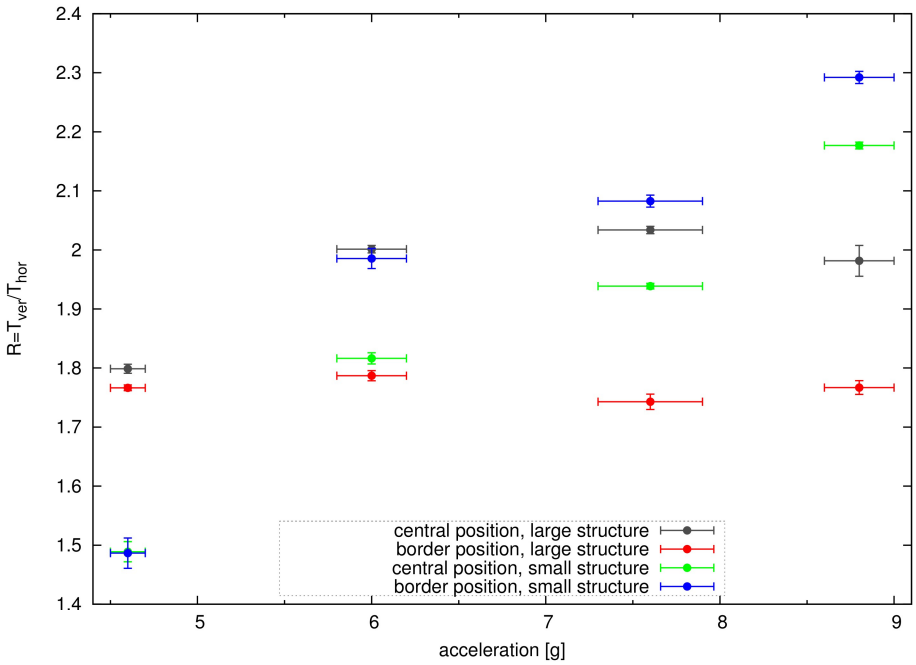

Figure 5.18.: The anisotropy R of the in depending on the acceleration, position and ground plate.

their difference increases. Moreover the value of R increases overall with the highest value being almost double the initial magnitude.

6. Discussion

6.1. Coefficient of Restitution

The precise value of $\epsilon = (0.930 \pm 0.002)$ gained in Section 3.8 (p. 17) suggests that the balls used are almost identical in this characteristic. The error seems too small considering the preciseness of the measuring setup. One reason could be that more uncertainty in the manual height measurement should be assumed; maybe, the human eye cannot detect the position of the ball with an error of few pixels only.

The ITTF publication [9] specifies for all commercial table tennis balls a value of $\epsilon \in [0.887; 0.923]$ which shall be measured with a similar method than the one used. Therefore, it is surprising that the measurement exceeds the specified amount. However, the value only lies outside the interval by roughly one percent.

6.2. Image Processing

The error of distance mentioned in Section 4.9.1 (p. 35) was intended to yield a lower bound for the error of position. The attained value for the error of 0.83 mm seems very low. This reflects the fact that the images were taken under ideal conditions as compared to the image taking process in the actual experiment. This error constitutes a minimum uncertainty characteristic to the experimental setup which should always be assumed. Thus, it is normal that this error is again smaller than the error found for the randomly selected images. It shall be noted that some publications exist, such as [10], that study the resolution limit only.

The error of the absolute position leads to the error of the velocities studied and is, therefore, the most interesting error. The achieved value which lies in the $0.1\,\mathrm{m\,s^{-1}}$ range for some sample data seems to be quite good considering the images were not, unlike those for the error of distance, taken under ideal conditions. Again, the assumption that manual measurement is precise might not be true. Nevertheless, the error was not expected to be so low when the first images were processed with

a simpler image processing routine which shows that improvement of the results is possible without dramatically adjusting the experimental setup.

As the main goal for the results of this Work are the different velocity distributions, it would be very interesting to analyse how the error of every computed velocity vector actually affects the outcome and preciseness of the distribution. This, however, would most likely include rigorous mathematical considerations in order to arrive at a satisfying result.

The error in horizontal direction seems to be random, yet the error in vertical direction is a constant shift to the top of the box and is, therefore, systematic. This illustrates one of the main insufficiencies of the entire experimental set up; the light intensity decreases to the bottom of the container and is most likely the sole reason for the direction of the vertical error.

6.3. Particle Density

The particle density is governed by the choice of ground plate and the acceleration whereas the position seems to play a minor role. The fluctuations in the horizontal direction are mostly within the accuracy that is expected of this kind of analysis. For both border positions in figures 5.4 (p. 49) and 5.5 (p. 50), the density rises at the margin which could be due to balls which collide with the window thereby reducing their velocity. In turn, they would be visible longer and the density count would increase. However, the plots of selected vectors in the bordering region of the window in figure 5.11 show that if this effect exists its magnitude is marginal. Both plots only illustrate that the symmetry of the distribution increases for higher accelerations, yet the density seems less affected by the acceleration.

The particle density plots for the small structured ground plate show clearly, however, that the goal to create gas of uniform density was not achieved for all but the highest acceleration.

6.4. Velocity Distribution

Overall, the differences in the velocity distributions can be explained with regard to the acceleration and the ground plates. Between 6.0 g and 8.8 g, the large structured ground plate, however, displays less of a shift towards higher velocities with increasing acceleration than the small structured ground plate. For the large structured

plate it might be interesting to analyse the range between 4.6 g and 6.0 g with one or more intermediate accelerations to see whether a sudden rise in higher velocities occurs or not. Above 6.0 g, the form of the distribution only changes slightly, yet the temperature still rises.

It remains rather unclear why the distribution of the large structured ground plate is more dependant on the position. A clear difference is visible in Figure 5.6 (p. 51) and the central position's spatial distribution features significantly higher velocities as well. Seemingly, for this ground plate, the position is a major factor, however, it is not totally transparent why. The small structured ground plate displays almost identical distributions for both positions in Figure 5.7 (p. 52) and the spatial distributions only differ slightly, too. For v_x, the difference in magnitude of high and low velocities between the two plates can be explained with the different size of the structure, the large structured plate simply excites the particles more intensively in the x-direction.

Moreover, the different dependencies on the acceleration for the vertical velocity v_y show that the small structured ground plate is more dependant on the acceleration. Here, the amount of faster velocities seems to be proportional to the acceleration as shown in Figure 5.9. The large structured ground plate features this effect only slightly and, again, the difference from (6.0 to 8.8) g is marginal. Nevertheless, the different magnitudes of v_y comparing the two plates is obvious, although no apparent reason is visible. Instead, one would rather expect the small structured plate to excite less in x-, yet more in y-direction in comparison to the large structured plate. Maybe, the rigidity of the small structured ground plate is the determining factor.

Overall, the results in this section seem satisfying. Further data might be acquired for the large structures ground plate below the lowest acceleration and from (4.6 to 6.0) g. The small structured ground plate would require even higher accelerations which are not possible to attain with the current setup.

6.4.1. The Velocity Distribution v_z

The v_z-distribution shows almost no fast entries, and has a totally different qualitative form as the v_x-distribution. It is expected to find similar distributions because the directions are regarded as equivalent. Both are equally affected by the ground plates, shaking acceleration and gravity. This leads to the conclusion that the indirect method of evaluating v_z did not succeed which is especially confusing taking into account that the error of the diameter detection is just as low as the the positional

errors.

One distinction between x- and z-direction, however, can be found; the dimension of the container is wider (x) than deeper (z) by a factor close to two. Maybe the container is not large enough in this direction. In the y-direction the acrylic glass box is not considerably higher, however, gravity and acceleration from the shaker apply differently. This seems to be the only explanation to decrease the confusion about this result.

6.4.2. Temperature

The term $\langle v^2 \rangle$ which is proportional to the temperature rises with the acceleration and is higher for the large structured ground plate which is not surprising bearing the velocity distribution and particle density in mind. These values confirm, like those of the the density for example suggest, that the small structured ground plate with the highest acceleration leads to a state which is comparable to the large structured ground plate with the lowest acceleration. However, this is not the case for the value of R where this analogy does not hold.

It remains unclear why the computed values for the large structured ground plate in the border position tend to be constant for the three highest accelerations. This is rather not expected, and the central view displays a qualitatively different behaviour.

Both Maxwell and Sonine-polynomial fit of the data do not show good results. For the Sonine fit, the difference to the individual data points is especially high left of the maxima where the fits are to high by a factor of two or more in some cases. In case of the Maxwell fit, this applies for both sides of the maximum. Both fits also overestimate the maxima considerably. That the fit accurately describes the data for higher velocities is no surprise considering the mathematical form of the distribution functions.

It was expected to find a non-Maxwell velocity distribution, yet it seems that the Sonine-Expansion, too, would require a lot more higher terms in order to reproduce the given data. Of course the Sonine fit is slightly better, but the more fit parameters are available, the better the fit matches independent of how good the model actually describes the data. It would be interesting to have an estimate of the error of the distribution data, however, considering the error of the individual velocities, it appears that the fits are just not expressing the data, rather than the data being overly inaccurate. The error for the distribution data would need to be that of an entire bin-width in order to match the fit at some points.

The quality of the fit can also be estimated by comparing the term $\langle v^2 \rangle$ found analysing the data directly and by fitting it. Here, the differences are very high as well. In one case the difference amounts to roughly 40 %. The relative difference to the analytical value of the first non-trivial Sonine-coefficient is even more striking with a factor well above five even between the absolute value of $a_2 = -0.012$ and the closest of the fit being 0.09.

6.5. Anisotropy

The number of data points in this section do not allow for a trend of the value of R to be guessed. However, the magnitude of R can be roughly estimated to lie around $R = 2$ for the data analysed. Even though the values for the small structured ground plate rise monotonic, it would be presumptuous to conclude such a constant and clear relation between R and the acceleration.

The almost constant value for the large structured ground plate above 6 g derives from the fact that the Temperature is not rising for this sample (see Table 5.2 , p. 57). However, the constant temperature itself can not be reasoned satisfyingly.

It should be noted that the error of R seems very low for most of the data points. This might lead to the question whether another method for estimating the error should be considered because the confidence of the data is unlikely to be this good.

6.6. Conclusion

The aim of this Work was to create and analyse a granular gas, and overall this task was completed in a satisfying manner. The experimental setup provided the circumstances to create the gas and the image processing successfully gained the position and velocity information which was transformed into the visibly available form of tables and plots. This, in turn, showed that the velocity distributions are, overall, those of a granular gas and the major dependencies between acceleration and ground plates, which could be expected, were affirmed by the gained results. Therefore, the setup and the results of this Work are a good starting point for future experiments.

7. Outlook and Future Work

For future work we suggest two major improvements. First of all, the lighting conditions should be improved. On the one hand, this means to intensify the overall luminosity to sharpen the contrast between the balls' border and the background. On the other hand, the gradient in lightning should be at least decreased further if not removed. This could be achieved by setting one of the floodlights up differently, e.g. letting the beam enter from below. This was not possible with the used frame, however, could probably attained if planned correctly. Second of all, the position of the camera in the z-direction should be adjusted. If possible, the entire container should be analysed and physical characteristics could be determined for more locations in the box. In addition, it would be interesting to turn the container in the x-z-plane and test whether the v_z-distribution would maintain its form, or if v_x would take its place. This would allow to determine if the present form of the v_z-distribution has some physical reason or can be solely attributed to the image processing.

Moreover, the range of the analysed accelerations could be bettered. The velocity distribution of the large structured ground plate shows a more significant change in form from the lowest to the second lowest acceleration than to the following accelerations. Thus, it might be interesting to investigate the range between those points, and below the lowest acceleration. However, the most dominant factor seems to be the structure of the ground plate itself which leads to the demand for other structures. Of special interest could be ground plates of the identical structure but with different sizes to gain a quantitative understanding of how the structure size affects the granular gas.

The image processing could also be improved at certain points. A method working with the greyvalue gradient field could not only detect a dynamic threshold but also aid in detecting particles; balls that are not visible enough to gain the *area* status because they are overshadowed by other particles could be found this way. Their position might not be attained but the noticed presence would improve the density

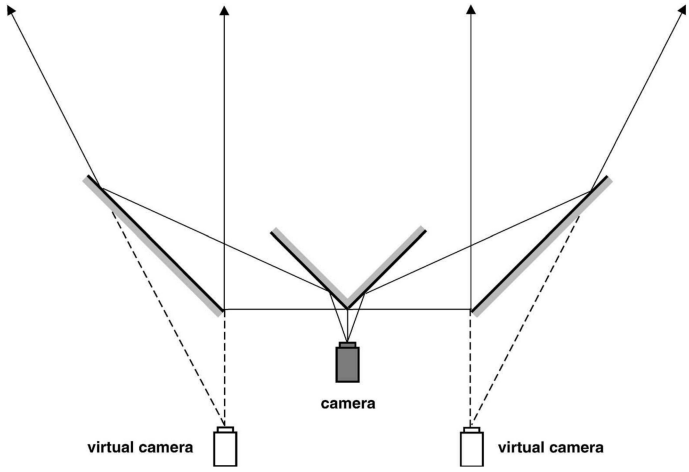

Figure 7.1.: The principle of stereo retrification taken from [6].

calculations.

Over the course of developing the image processing program it was also considered and tried to find balls with a Hough-transformation of the images. This method is not directly included in the used version of Matlab[1]. However, some user supplied implementations exist which are mainly working on images with lower quality. Thus, this method would have to be implemented for the project, or, more precisely, its images, individually. It has to be noted again that the images do not depict circles but plane balls with the intensity gradient mentioned above.

Nevertheless, the transformation has the potential to compute the centre of balls which are not entirely visible because of other balls being partially in front of them or only a fraction of the particle itself positioned inside the image. Correctly implemented, this would strip the density of its sudden decrease in the margin grid boxes. Because the computation time is significantly higher than that of the erosion (seconds vs. tenth of a second)[2] and the time needed rises with the size of the image, a combination of both methods might be useful where large regions and the border are treated with extra effort.

If the setup was to be rebuild incorporating major changes, the following two ideas come to mind. First of all, a method to precisely measure the z-component of the balls could be implemented using the methods of stereovision-correspondence-analysis (see for example [6]) where two images taken from slightly different angles

[1] The latest version (2012) features a function called imfindcircles which apparently identifies circles in images.

[2] This value is observed using the mentioned implementations; it might improve significantly if the image is appropriately treated.

are used to construct a three dimensional image by finding corresponding points in the two images. This could either be realised by setting up two cameras at different angles. However, it would be necessary to synchronise the two devices precisely. Or a setup of mirrors or prisms could be installed in front of the sole camera's lens and split the image in two parts. A 90° mirror might split the beam and send each to a plane mirror pointing towards the container. The result in a setup like the one depicted in Figure 7.1, and would almost behave like having taken two separate images from different angles. Because only half the image size is available, the camera would need to be placed considerably further apart from the container. In turn, this would make more framework necessary to hold additional cover averaging the lighting conditions.

Another interesting question that is predicted by theory and simulation [3], is the correlation of translation and rotation in a granular gas which seems to exist even for low particle roughness. If the lighting was intense and even enough for darker balls to be distinguished, painted balls would become an option as well. Such painted particles could feature some kind of pattern in order to determine rotational direction and magnitude. In this case, the mentioned less expensive balls would regain attention because of their apparent rougher surface.

Overall, the setup and the results of this Work are regarded as viable starting points for future experiments.

A. Supplementary Figures

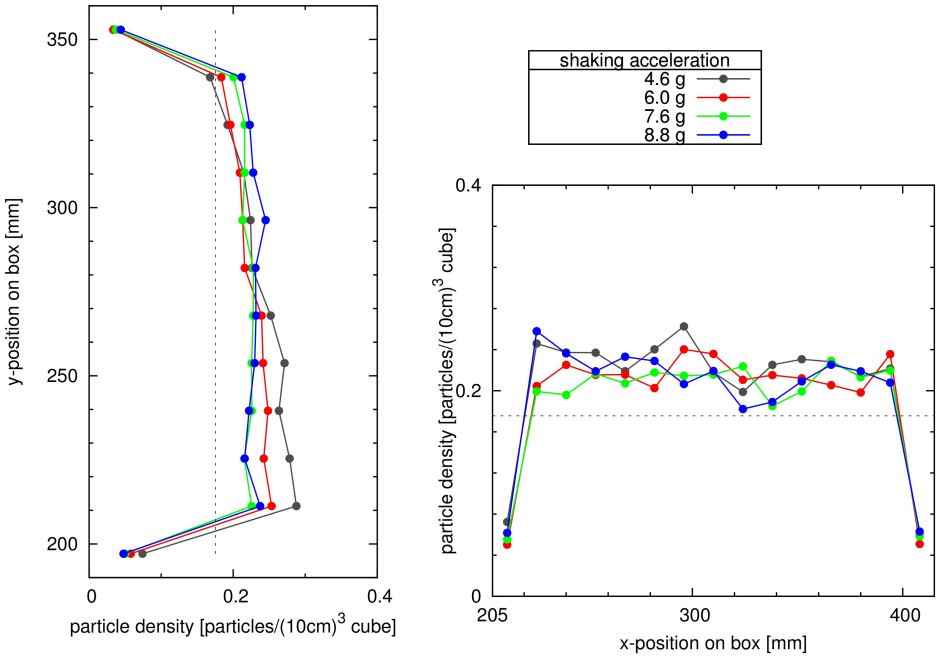

Figure A.1.: Example of a density plot with all observed data included. The decrease in magnitude at towards the margins is clearly visible,however, is an artefact of the image processing and bears not physical meaning. The data is computed using the large structured ground plate in central position.

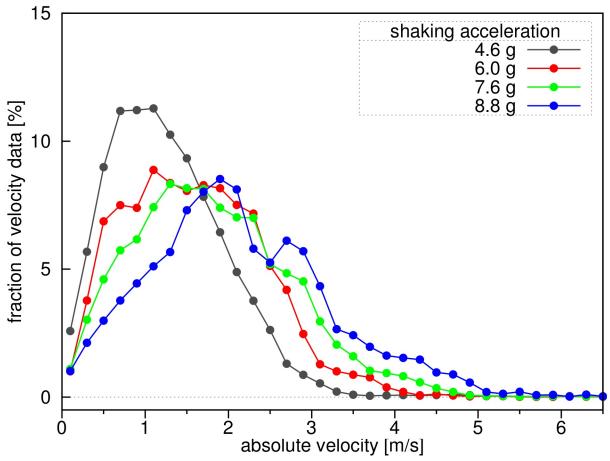

Figure A.2.: Velocity distribution for the large structured ground plate in a central position.

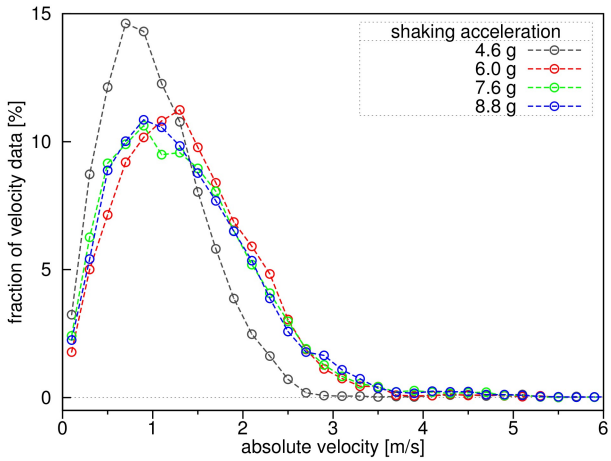

Figure A.3.: Velocity distribution for the large structured ground plate in a border position.

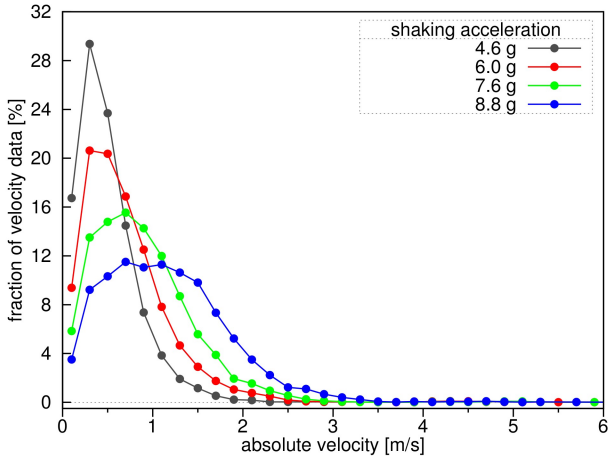

Figure A.4.: Velocity distribution for the small structured ground plate in a central position.

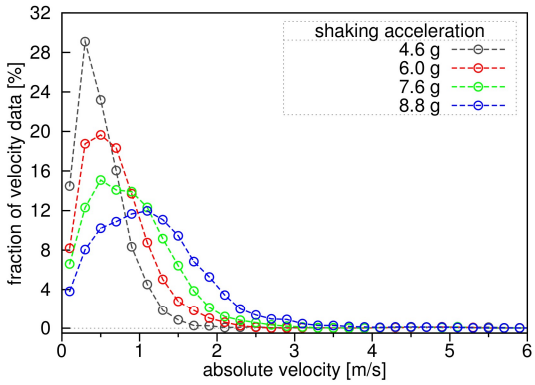

Figure A.5.: Velocity distribution for the small structured ground plate in a border position.

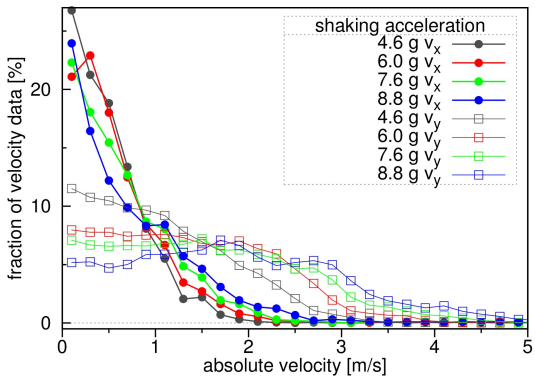

Figure A.6.: Spatial velocity distribution for the large structured ground plate in a central position.

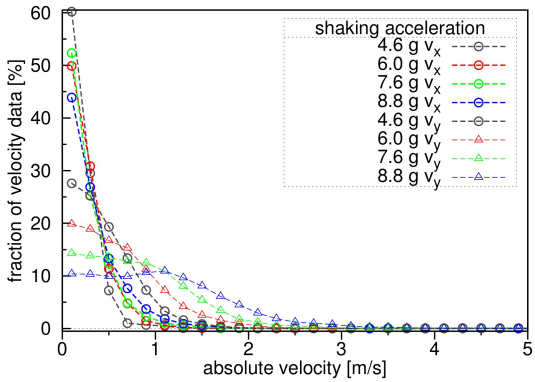

Figure A.7.: Spatial velocity distribution for the small structured ground plate in a border position.

B. Supplementary Tables

x-position	z-position	shaking amplitude I $[A]$	voltage U $[m\mathrm{V}]$	a $[g]$
centre	centre	45	456	4.58
		60	580	5.83
		75	712	7.15
		90	843	8.47
left	centre	45	470	4.72
		60	630	6.33
		75	760	7.64
		90	899	9.03
right	centre	45	460	4.62
		60	620	6.23
		75	750	7.54
		90	891	8.95
centre	front	45	460	4.62
		60	587	5.90
		75	780	7.84
		90	889	8.93
centre	back	45	463	4.65
		60	587	5.90
		75	776	7.80
		90	874	8.78

Table B.1.: Acceleration a measured on the metal ground plate. The factor of Conversion for the acceleration sensor is given by f =49.76 mV/g The reference value for g is g=9.807 $\mathrm{m\,s^{-2}}$

x position [cm]	x	y	distance	diameter	distance [mm]	$\sigma_{distance}$ [mm]	$\sigma_{distance}$ [%]
y=22 cm z=centre							
8	95.5	838.3	280.94	196	57.48	-0.37	0.6
	376.4	843.3		195			
11	239.6	840	285.74	197	57.87	0.02	0.0
	525.3	844.6		198			
15	428.1	838.8	286.47	197	58.17	0.32	0.5
	714.5	845.1		197			
19	623.5	841.4	286.33	196	58.43	0.58	1.0
	909.8	845.3		196			
24	872.6	841.1	285.32	198	57.64	-0.21	0.4
	1157.9	844.6		198			
y=34 cm z=centre							
9	75.1	262.9	267.05	193	55.20	-2.65	4.6
	342	271.9		194			
11	240.7	267.2	274.75	194	56.50	-1.35	2.3
	515.4	272.6		195			
15	424	267	278.02	194	57.32	-0.53	0.9
	702	270		194			
18	553.2	278.3	283.09	195	58.22	0.37	0.6
	836.2	285.3		194			
24	848.7	281.3	282.14	194	58.02	0.17	0.3
y=22 cm z=back							
	1130.8	286.1		195			
9	199.4	801.4	247.85	175	57.15	-0.70	1.2
	447.2	806.6		172			
12	323.9	801.5	248.16	171	57.88	0.03	0.1
	572	806.8		172			
15	456.8	802.5	249.53	175	57.53	-0.32	0.5
	706.3	806.6		172			
19	629.5	803.2	250.03	172	57.98	0.13	0.2
	879.5	806.9		173			
24	843.7	803.7	249.73	173	57.91	0.06	0.1
y=34 cm z=back							
	1093.4	807.5		172			
9	173.9	303.5	249.40	171	58.17	0.32	0.6
	423.2	296.4		172			
15	431.8	300.4	250.17	171	58.52	0.67	1.2
	681.9	294.6		171			
19	617.7	299	251.21	170	58.93	1.08	1.9
	868.9	300.8		171			
24	812.5	299	250.55	171	58.44	0.59	1.0
y=22 cm z=front							
	1063	294.2		172			
12	226.28	896.06	337.04	231	57.87	0.02	0.0
	563.09	908.48		235			
15	392.84	894.27	335.58	231	57.86	0.01	0.0
	728.19	906.56		233			
19	621.27	900.04	338.10	234	57.67	-0.18	0.3
y=34 cm z=front							
	959.21	910.37		235			
15	324.59	213.85	335.73	236	56.31	-1.54	2.7
	660.15	224.59		241			
19	596.41	231.90	338.18	240	56.01	-1.84	3.2
	934.58	234.44		243			

Table B.2.: Data used for calculating the error of the distance between two balls glued to a metal block. All data in px if not otherwise stated. The left column indicates the position of the metal block described in Section 4.9.1 (p. 35). The error is greater for balls higher (y=34 cm) at the front window. This might be due to less sharpness and the fact that the lighting increases with increasing height which could intensify the effect.

image processing				by hand			
position				position			
x	y	width	height	x	y	width	height
366.6	247.1	175	181	364.5	254	177	180
481.9	663	177	177	481	667.5	182	179
512.9	472.7	178	178	512.5	476.5	177	183
811.5	857.8	235	233	810.5	860	235	238
336.7	255.9	172	172	333.5	264.5	177	181
496.1	675.8	182	179	496	679.5	184	179
559.2	506.3	180	178	558.5	508	183	180
821.4	887.2	232	233	820.5	889	231	234
306.3	269.4	174	172	307	275.5	172	179
503.9	730.8	184	179	502.5	734.5	185	181
613.8	501.3	181	178	614	504.5	186	183
831.4	919.6	233	226	829.5	918	233	230
275.7	284.4	172	175	274.5	291	177	176
511	789.9	175	178	509.5	795.5	177	183
669.2	499.3	182	185	668.5	503	185	186
1184.7	224.2	204	199	1186.5	227.5	203	203
245.8	303.5	173	175	245.5	310	179	180
517.8	852.4	177	177	517	860	180	180
725.8	500.6	185	178	724	505.5	184	187
1130.3	190.2	201	199	1128.5	191.5	199	203
215.6	323.6	174	177	214.5	328.5	177	175
524.1	916.9	178	179	523.5	922.5	175	185
782	503.8	186	187	781.5	509.5	189	191
1077.2	158	199	195	1076.5	161	199	200
185.3	345.6	175	167	180	350.5	176	175
838.8	510.3	188	180	836	515.5	184	185
1025.2	128.5	196	197	1022.5	132.5	197	199
154.8	368.4	174	175	152	375.5	180	177
896.2	519.6	189	188	896	524	190	190
123.9	392.8	171	172	121	402.5	176	177
954.2	532	188	182	950.5	539.5	187	189
108.4	420.2	175	175	104	429	176	176
1012.6	550.4	190	187	1011.5	558	191	190
125.3	445.9	177	175	123.5	453	179	180
1184.2	176.1	230	239	1229	226	236	236
1071.5	574.1	194	189	1070.5	577.5	193	187
143.8	473.3	178	171	142	478	180	176
787.2	297.8	178	170	786	305.5	176	181
844.6	97.9	194	184	845.5	105.5	195	199
1131.3	599.3	195	190	1131.5	600.5	189	189
1171.2	184.7	233	231	1165.5	187.5	225	225
161.4	503.6	179	182	160.5	508.5	179	183
779.2	82.1	202	203	811	111	196	200
763	364.8	177	172	761.5	371.5	177	183
1174.9	214.4	226	228	1168.5	216.5	221	225
1191.7	629.2	193	191	1186.5	631.5	187	193

Table B.3.: Positions and width and height produced by image processing measured by hand as explained in Section 4.9.2 (p. 37) for the same balls. Note that the data is given in image coordinates [px] where the upper left corner is the point (0;0).

differences				absolute differences				
Δx	Δy	Δwidth	Δheight	Δ|x|	Δ|y|	Δ|width|	Δ|height|	distance
2.1	6.9	-2.0	1.0	2.1	6.9	2.0	1.0	7.2
0.9	4.5	-5.0	-2.0	0.9	4.5	5.0	2.0	4.6
0.4	3.8	1.0	-5.0	0.4	3.8	1.0	5.0	3.8
1.0	2.2	0.0	-5.0	1.0	2.2	0.0	5.0	2.4
3.2	8.6	-5.0	-9.0	3.2	8.6	5.0	9.0	9.2
0.1	3.7	-2.0	0.0	0.1	3.7	2.0	0.0	3.7
0.7	1.7	-3.0	-2.0	0.7	1.7	3.0	2.0	1.8
0.9	1.8	1.0	-1.0	0.9	1.8	1.0	1.0	2.0
-0.7	6.1	2.0	-7.0	0.7	6.1	2.0	7.0	6.1
1.4	3.7	-1.0	-2.0	1.4	3.7	1.0	2.0	4.0
-0.2	3.2	-5.0	-5.0	0.2	3.2	5.0	5.0	3.2
1.9	-1.6	0.0	-4.0	1.9	1.6	0.0	4.0	2.5
1.2	6.6	-5.0	-1.0	1.2	6.6	5.0	1.0	6.7
1.5	5.6	-2.0	-5.0	1.5	5.6	2.0	5.0	5.8
0.7	3.7	-3.0	-1.0	0.7	3.7	3.0	1.0	3.8
-1.8	3.3	1.0	-4.0	1.8	3.3	1.0	4.0	3.8
0.3	6.5	-6.0	-5.0	0.3	6.5	6.0	5.0	6.5
0.8	7.6	-3.0	-3.0	0.8	7.6	3.0	3.0	7.6
1.8	4.9	1.0	-9.0	1.8	4.9	1.0	9.0	5.2
1.8	1.3	2.0	-4.0	1.8	1.3	2.0	4.0	2.2
1.1	4.9	-3.0	2.0	1.1	4.9	3.0	2.0	5.0
0.6	5.6	3.0	-6.0	0.6	5.6	3.0	6.0	5.6
0.5	5.7	-3.0	-4.0	0.5	5.7	3.0	4.0	5.7
0.7	3.0	0.0	-5.0	0.7	3.0	0.0	5.0	3.1
5.3	4.9	-1.0	-8.0	5.3	4.9	1.0	8.0	7.2
2.8	5.2	4.0	-5.0	2.8	5.2	4.0	5.0	5.9
2.7	4.0	-1.0	-2.0	2.7	4.0	1.0	2.0	4.8
2.8	7.1	-6.0	-2.0	2.8	7.1	6.0	2.0	7.6
0.2	4.4	-1.0	-2.0	0.2	4.4	1.0	2.0	4.4
2.9	9.7	-5.0	-5.0	2.9	9.7	5.0	5.0	10.1
3.7	7.5	1.0	-7.0	3.7	7.5	1.0	7.0	8.4
4.4	8.8	-1.0	-1.0	4.4	8.8	1.0	1.0	9.8
1.1	7.6	-1.0	-3.0	1.1	7.6	1.0	3.0	7.7
1.8	7.1	-2.0	-5.0	1.8	7.1	2.0	5.0	7.3
-44.8	49.9	-6.0	3.0	44.8	49.9	6.0	3.0	67.1
1.0	3.4	1.0	2.0	1.0	3.4	1.0	2.0	3.5
1.8	4.7	-2.0	-5.0	1.8	4.7	2.0	5.0	5.0
1.2	7.7	2.0	-11.0	1.2	7.7	2.0	11.0	7.8
-0.9	7.6	-1.0	-15.0	0.9	7.6	1.0	15.0	7.7
-0.2	1.2	6.0	1.0	0.2	1.2	6.0	1.0	1.2
5.7	2.8	8.0	6.0	5.7	2.8	8.0	6.0	6.4
0.9	4.9	0.0	-1.0	0.9	4.9	0.0	1.0	5.0
-31.8	28.9	6.0	3.0	31.8	28.9	6.0	3.0	43.0
1.5	6.7	0.0	-11.0	1.5	6.7	0.0	11.0	6.9
6.4	2.1	5.0	3.0	6.4	2.1	5.0	3.0	6.7
5.2	2.3	6.0	-2.0	5.2	2.3	6.0	2.0	5.7

Table B.4.: Differences between the value produced by the image processing program and manually measured data which are both displayed in Table B.3 on the previous page. Note that the data is given in image coordinates [px] where the upper left corner is the point (0;0).

Ball	L1		H1		L2		H2		L3		H3		L4		H4	
	982	2	13	2	951	3	155	1								
			90	1	945	3	215	2	950	1	314	1				
	947	1	393	1	981	2	475	1	281	2						
used	950	2	176	1	952	3	277	2	962	3						
	942	3	196	1	943	3	300	1	953	4	389	2				
	944	4	187	2	950	5	287	2	957	6	374	3				
	943	5	201	1	934	3	306	1								
used			216	2	942	3	318	3	944	5	402	2	948	3	468	3
	960	3	384	2	966	2	467	2	979	4	538	2	989	5	600	2
	949	4	238	2	953	3	333	2	967	4	418	2	973	4	488	3
	938	3	297	1	940	2	386	1	937	2	476	1	937	4	559	6
	951	5	432	2	964	3	513	2	974	4	580	4	986	3	636	3

Table B.5.: Manually measured extremal positions of balls used for calculation of the coefficient of restitution ϵ. Ln indicates the nth minimal position on the ground plate whereas Hn stands for the nth climax position. Behind the position's value an error is given according to Section 3.8. All data is measured in pixels. A single line in the table corresponds to one dropping of the ball and filming thereof.

Ball	Height 1		Height 2		Height 3		Height 4	
	969	3	796	3				
	855	1	730	4	636	1		
	554	1	506	2	281	2		
used	774	2	675	4	962	3		
	746	3	643	3	564	4		
	757	4	663	5	583	7		
	742	5	628	3				
used			624	4	542	5	480	4
	576	4	499	3	441	4	389	5
	711	4	620	4	549	4	485	5
	641	3	554	2	461	2	378	7
	519	5	451	4	394	6	350	4

Table B.6.: Heights gained from the extremal positions given in Table B.5. Height n is the nth height given by Height n =Hn−Ln. The error is computed as in Equation 3.3 (p. 18) All data is given in pixels.

ball	ϵ_{12}	$\sigma_{\epsilon_{12}}$	ϵ_{23}	$\sigma_{\epsilon_{23}}$	ϵ_{34}	$\sigma_{\epsilon_{34}}$
	0.91	0.006				
	0.92	0.006	0.93	0.006		
	0.96	0.006	0.75	0.015		
used	0.93	0.007	1.19	0.004		
	0.93	0.008	0.94	0.011		
	0.94	0.011	0.94	0.016		
	0.92	0.010				
used			0.93	0.014	0.94	0.015
	0.93	0.010	0.94	0.013	0.94	0.019
	0.93	0.010	0.94	0.011	0.94	0.015
	0.93	0.007	0.91	0.008	0.91	0.024
	0.93	0.015	0.93	0.019	0.94	0.021

Table B.7.: Values of the coefficient of restitution calculated from data presented in Table B.6. ϵ_{nj} is calculated from Height n and Height j of that table using the Equation 2.3 (p. 5). The error is given on the right of the respective value and evaluates as explained in Equation 3.2 (p. 18). The two statistical outliers are left out of the calculation of the weighed mean.

Bibliography

[1] N. V. Brilliantov and T. Pöschel. Breakdown of the sonine expansion for the velocity distribution of granular gases. *EPL (Europhysics Letters)*, 74(3):424, 2006. URL `http://stacks.iop.org/0295-5075/74/i=3/a=424`.

[2] N. V. Brilliantov and T. Pöschel. *Kinetic Theory of Granular Gases*. Oxford Graduate Texts. OUP Oxford, 2010. ISBN 9780199588138.

[3] Nikolai V. Brilliantov, Thorsten Poeschel, W. Till Kranz, and Annette Zippelius. Translations and rotations are correlated in granular gases. *Phys. Rev. Lett.*, (98), September 2006. URL `http://arxiv.org/abs/cond-mat/0609213`.

[4] Albert Einstein. *Investigation on the Theory of the Brownian Movement*. Dover, 1956.

[5] Eric Falcon, Stephan Fauve, and Claude Laroche. Experimental study of a granular gas fluidized by vibrations, September 2000. URL `http://arxiv.org/abs/cond-mat/0009172`.

[6] Joshua Gluckman and Shree K. Nayar. Rectified catadioptric stereo sensors. *IEEE Trans. Pattern Anal. Mach. Intell.*, 24(2):224–236, February 2002. ISSN 0162-8828. doi: 10.1109/34.982902. URL `http://dx.doi.org/10.1109/34.982902`.

[7] I. Goldhirsch and G. Zanetti. Clustering instability in dissipative gases. *Phys. Rev. Lett.*, 70:1619–1622, Mar 1993. doi: 10.1103/PhysRevLett.70.1619. URL `http://link.aps.org/doi/10.1103/PhysRevLett.70.1619`.

[8] Isaac Goldhirsch. Introduction to granular temperature. *Powder Technology*, (182), 2008.

[9] ITTF. The ball (version for 40mm balls) technical leaflet t3. Technical report, The International Table Tennis Federation (ITTF), Chemin de la Roche, 11 1020 Renens/Lausanne, Switzerland, 2009. URL `http://www.ittf.com/stories/pictures/T3_40mmBall.pdf`.

[10] C. J. Kähler, S. Scharnowski, and C. Cierpka. On the resolution limit of digital particle image velocimetry. *Experiments in Fluids*, 52:1629–1639, June 2012. doi: 10.1007/s00348-012-1280-x.

[11] A. Kudrolli and J. Henry. Non-gaussian velocity distributions in excited granular matter in the absence of clustering. *Phys. Rev. E*, 62:R1489–R1492, Aug 2000. doi: 10.1103/PhysRevE.62.R1489. URL `http://link.aps.org/doi/10.1103/PhysRevE.62.R1489`.

[12] Nobuyuki Otsu. A threshold selection method from gray-level histograms. *IEEE Transactions on Systems, Man, and Cybernetics*, 9(1):62–69, 1979.

Acknowledgements

I would like to express my gratitude to all those who gave me the possibility to complete this Thesis. First of all, I would like to thank Dr. Matthias Schröter for offering and supervising this work. He aided me with stimulating suggestions, encouragement and helpful advises over the entire period of research and writing. Second of all, I wish to express my gratitude to Prof. Dr. Sarah Köster who kindly accepted to be the second referee.

Moreover, I am indebted to Chih-Wei Peng who worked on the experimental equipment before. He was so kind to introduce me to its usage and answer any questions at any time. Furthermore, I thank Wolf Keiderling for his practical advises and technical expertise which he always offered. The same holds true for the workshop team.

Markus Richter has to be thanked for his introduction and useful hints with regards to image processing, and for being a good colleague in our basement room. In addition, the suggestions of Max Neudecker regarding the treatment of some 11000-lines data files were very helpful.

Last but not least, I have to praise Andreas Sorge and Laura Syms for their meaningful proof-reading with regard to both content and language of this Thesis. Fellow students Torben Mende and Marius Müller also aided me with advice and suggestions after reading the Work.

Erklärung nach §13(8) der Prüfungsordnung für den Bachelor-Studiengang Physik und den Master-Studiengang Physik an der Universität Göttingen:

Hiermit erkläre ich, dass ich diese Abschlussarbeit selbständig verfasst habe, keine anderen als die angegebenen Quellen und Hilfsmittel benutzt habe und alle Stellen, die wörtlich oder sinngemäß aus veröffentlichten Schriften entnommen wurden, als solche kenntlich gemacht habe.
Darüberhinaus erkläre ich, dass diese Abschlussarbeit nicht, auch nicht auszugsweise, im Rahmen einer nichtbestandenen Prüfung an dieser oder einer anderen Hochschule eingereicht wurde.

Göttingen, den 31. Oktober 2012

(Jasper Ole Cirkel)